2172–2189 *Nucleic Acids Research, 2022, Vol. 50, No. 4* *Published online 12 February 2022*
https://doi.org/10.1093/nar/gkac086

The interaction between RPAP3 and TRBP reveals a possible involvement of the HSP90/R2TP chaperone complex in the regulation of miRNA activity

Yoann Abel[1,4,5,†], Christophe Charron[1,†], Camille Virciglio[1], Valérie Bourguignon-Igel[1], Marc Quinternet[2], Marie-Eve Chagot[1], Marie-Cécile Robert[3,4,5], Céline Verheggen[3,4,5], Christiane Branlant[1], Edouard Bertrand[3,4,5], Xavier Manival[1], Bruno Charpentier[1] and Mathieu Rederstorff[1,*]

[1]Université de Lorraine, CNRS, IMoPA, F-54000 Nancy, France, [2]Université de Lorraine, CNRS, INSERM, IBSLOR, F-54000, Nancy, France, [3]IGH, Université de Montpellier, CNRS, F-34090, Montpellier, France, [4]IGMM, Université de Montpellier, CNRS, F-34090, Montpellier, France and [5]Equipe labélisée Ligue Nationale contre le Cancer, University of Montpellier, CNRS, F-34090, Montpellier, France

Received February 25, 2021; Revised January 21, 2022; Editorial Decision January 25, 2022; Accepted January 27, 2022

ABSTRACT

MicroRNAs silence mRNAs by guiding the RISC complex. RISC assembly occurs following cleavage of pre-miRNAs by Dicer, assisted by TRBP or PACT, and the transfer of miRNAs to AGO proteins. The R2TP complex is an HSP90 co-chaperone involved in the assembly of ribonucleoprotein particles. Here, we show that the R2TP component RPAP3 binds TRBP but not PACT. The RPAP3-TPR1 domain interacts with the TRBP-dsRBD3, and the 1.5 Å resolution crystal structure of this complex identifies key residues involved in the interaction. Remarkably, binding of TRBP to RPAP3 or Dicer is mutually exclusive. Additionally, we found that AGO(1/2), TRBP and Dicer are all sensitive to HSP90 inhibition, and that TRBP sensitivity is increased in the absence of RPAP3. Finally, RPAP3 seems to impede miRNA activity, raising the possibility that the R2TP chaperone might sequester TRBP to regulate the miRNA pathway.

INTRODUCTION

MicroRNAs (miRNAs) play essential roles in regulating gene expression. Their biogenesis begins in the nucleus with the processing of a pri-miRNA by the microprocessor complex, composed of the type III Ribonuclease (RNase) Drosha and its cofactor DGCR8 (DiGeorge syndrome Critical Region 8), giving rise to the pre-miRNA. After cytoplasmic export via the exportin 5/Ran-GTP pathway, the pre-miRNA is further processed into the mature, double-stranded miRNA duplex by the cytoplasmic RNase III Dicer (1,2), which is associated with one of its two double-stranded RNA binding protein co-factors, TRBP (or TARBP2: TransActivation Response–TAR–RNA binding protein) or PACT (or PRKRA: protein activator of the double-stranded RNA-dependent kinase-PKR). Finally, one strand of the cleaved pre-miRNA is loaded onto an Argonaute protein (Ago) in the RNA induced silencing complex (RISC) (2).

As illustrated by their names, prior to their functions as co-factors of Dicer, both TRBP and PACT proteins were initially identified for their positive and negative roles in HIV infection, respectively. Indeed, TRBP has several positive effects on HIV multiplication. It was initially identified as a binding factor of the TAR RNA element of human immunodeficiency viruses HIV-1 and 2 (3). The 5′-terminal TAR stem-loop structure of HIV RNAs impedes efficient translation of the viral RNAs (4) and TRBP binding to this element relieves this negative effect. Interestingly, Dicer was also recently proposed to be involved in this process (5). TRBP was additionally shown to promote HIV infection by directly or indirectly inhibiting PKR activation, which is triggered by the TAR RNA and leads to global translation inhibition (6). More precisely, TRBP inhibits PKR activity via a direct interaction that is reinforced when TRBP is phosphorylated (7,8). Furthermore, PKR activity can also be impeded by TRBP through its binding to PACT, which prevents PACT's activating interaction with PKR. Finally, another important activity of TRBP in favor of HIV multiplication was recently discovered: TRBP recruits the 2'-*O*-methyltransferase FTSJ3 on HIV RNA (9), which subsequently methylates the viral genome at several specific positions enabling viral escape from the host's innate immune response.

*To whom correspondence should be addressed. Tel: +33 3 72 74 66 50; Email: mathieu.rederstorff@univ-lorraine.fr
†The authors wish it to be known that, in their opinion, the first two authors should be regarded as Joint First Authors.

TRBP and PACT are both composed of three double-stranded RNA binding domains (dsRBD), the two first ones are involved in double-stranded RNA (dsRNA) binding and classified as canonical type A dsRBDs, while the third one mediates protein–protein interactions, in particular with Dicer and corresponds to a non-canonical type B dsRBD (10,11). While TRBP contributes both to pre-miRNAs and pre-siRNAs processing by Dicer, PACT participates more efficiently to pre-miRNA processing, a specificity that was shown to be mediated by the N-terminal domain of the two cofactors (12). Additionally, association of Dicer to TRBP or PACT was shown to generate miRNAs of different sizes, and possibly of different target repertoire, referred to as isomiRs (10,13). Once the pre-miRNA has been cleaved in the cytoplasm, one of the single-strand derived from the mature miRNA duplex is loaded onto the AGO2 protein to form the RNA induced silencing complex (RISC), and this is efficiently stimulated by the HSC70/HSP90 chaperone machinery (14–18). These chaperones were shown to bind and stabilize free AGO2 (18) and to target it to processing bodies and stress granules (17). MiRNA-dependent translational repression and/or siRNA directed cleavage of Ago were also shown to be dependent on HSP90 (17,18).

Interestingly, the HSC70/HSP90 chaperones have numerous co-chaperones (19). Of particular interest is the R2TP co-chaperone complex, playing a crucial role in the assembly and maturation of large macromolecular complexes essential for most of the universally conserved nanomachines of eukaryotic cells (20–22). This includes several RNPs, such as the U4 and U5 snRNPs, telomerase, as well as the C/D and H/ACA snoRNPs involved in ribosome biogenesis (20–21,23–27). It also includes protein-only clients, such as the nuclear RNA polymerase II (28,29), dynein (30,31) or complexes containing any of the phosphatidylinositol 3-kinase–like family of kinases (PIKKs): mammalian Target Of Rapamycin (mTOR; (32,33), ATM and RAD3-related (ATR) interacting protein (ATRIP) (34), Suppressor with Morphogenetic effect on Genitalia (SMG1; (35), DNA-PK and TRRAP (36).

The R2TP complex consists of a RPAP3:PIH1D1 heterodimer associated to two hetero-hexamer of RUVBL1 and RUVBL2, which are related AAA + ATPases that also display chaperone activities (24). In metazoans, the R2TP is part of a larger chaperone complex called the PAQosome, which contains an additional series of prefoldin-like proteins and POLR2E and WDR92 (37). Within R2TP, PIH1D1 is believed to play important roles in specifying and recruiting clients, in part via its ability to specifically bind CK2 phosphorylation sites, i.e. phosphoserines embedded in acidic regions of DSDD/E consensus (32,38). RPAP3 regulates HSP90 activity (39,40) and also plays a scaffolding role as it makes stable interactions with all the other components of the R2TP complex (39). It binds HSP90 with its two TPR domains, PIH1D1 via a small peptide sequence located immediately after the TPRs, and the RUVBL1/2 hetero-hexamers with its conserved C-terminal domain (41–44). However, RPAP3 has not so far been involved in client recognition.

Here, we identified a direct interaction between the TPR1 domain of RPAP3 and the dsRBD3 of TRPB (10,45) and showed that this interaction is exclusive from that of TRBP with Dicer. Remarkably, RPAP3 depletion increased miRNA-dependent translational repression of a luciferase reporter, indicating that its direct association with TRBP could be involved in preventing its function in miRNA processing or activity. The X-ray structure of the TRBP/RPAP3 complex at a resolution of 1.5 Å provides a rational for these effects and brings exciting novel insights towards understanding structural and molecular features of chaperones in dsRNA pathways.

MATERIALS AND METHODS

Cell culture

HeLa and HEK293T (including T-Rex cell lines) cells were maintained in Dulbecco's modified Eagle's medium. HCT-116 cells were maintained in Mc'Coys medium. Both media were supplemented with 10% of fetal bovine serum, 10 U/ml of penicillin/streptomycin and 2.9 mg/ml of glutamine, in a humidified 5% CO_2 incubator at 37°C. Additionally, T-Rex cells were maintained with 100 μg/ml of zeocin and 10 μg/ml of blasticidin.

Generation of stable, inducible, Flag T-REX cell lines

Inducible T-Rex cell lines were generated following the manufacturer's instructions (Invitrogen). Briefly, confluent HEK-293 T-Rex cells were transfected in 10 cm cell culture plates in blasticidin containing medium (no zeocin) with 9 μg of the pOG44 plasmid enabling expression of the Flp recombinase and 1 μg of the pcDNA5/FRT plasmid containing the flagged protein of interest gene (RPAP3 or TRBP). Medium was changed after 2 days with blasticidin containing medium. The next day, cells were split and treated with 100 μg/ml of hygromycin B. The blasticidin/hygromycin medium is changed every 4 to 5 days, during two weeks, until isolated clones can be retrieved and transferred to a new dish for screening.

HCT-116 RPAP3-AID* cells generation

HCT-116 cells, provided by the Cancer Research Institute of Montpellier (IRCM) cell culture unit, were co-transfected in 6-well plates with the CRISPR repair pUC57 plasmid, containing RPAP3 Cter homologous DNA sequences for the homologous recombination, as well as the AID*-3xHA IRES and a Neomycin selection marker. CRISPR guide vector pUC57 attbU6 and Cas9 vector pX335 U6 hSpCas9n (D10A) (Addgene 42335) were transfected as follow : 0.28 μg of Cas9 vector, 0.85 μg of RPAP3 guide RNA expression vector, 0.85 μg of RPAP3 repair donor vector, 4 μl of JetPrime (Ozyme) and 200 μl of JetPrime Buffer. Mc Coy's medium was changed after 24 h of transfection and 24 h later the modified cells were selected by adding neomycin at 800 μg/ml. Ten days later, individual clones were amplified and finally characterized by PCR and western blot.

HCT-116 OsTIR1 RPAP3-AID* cells generation

About 300 μl of viral particles containing pBABE puro-OsTIR1 9*Myc vector (provided by Bénédicte Delaval,

CRBM – Montpellier) were used to infect HCT-116 RPAP3-AID* cells and HCT-116 WT cells in 12-well plates (5000 cells/well) grown for 24 h in Mc Coy's medium without FBS. After 2 h, 1 ml of Mc Coy's medium with FBS was added. Medium was changed after 24 h. Seventy-two hours later, cells were selected by adding 2 μg/ml of puromycin for at least 10 days. Cells were finally characterized by PCR and western blot (46,47) (Supplementary Figure S8).

Plasmids and cloning

DNA cloning was performed using standard techniques or with Gateway™ system (Invitrogen). For NMR and crystallogenesis assays, TRBP and RPAP3 ORFs were cloned in pnEA-3CH and pnCS vector (respectively) at the *5′-NdeI* and *3′-BamHI* sites (48,49). For co-expression assays, RPAP3, TRBP, Dicer and PACT ORFs were cloned in pnEA-3CH, pnCS and pnYK plasmids modified to become compatible with the Gateway cloning technology. For that, the *ccdb* and *chloramphenicol* genes were amplified by PCR in pDEST17 and inserted in these vectors at the *5′-NdeI* and *3′-BamHI* sites. pnYK vector was created from pnYC vector (48) by homologous recombination between the chloramphenicol and kanamycin genes resistance gene using the In-Fusion kit (Clontech) following the manufacturer's recommendations. For GST pull-down experiments, ORFs were cloned in pDEST15 (containing the GST tag) and pDEST17 Gateway (containing the His_6 tag) vectors (Thermo Fisher Scientific). For Y2H assays, pACT2, pAS2 and pGBKT7 were used. For co-immunoprecipitation, the TRBP ORF was cloned into the pcDNA3.1 and nV5-DEST plasmids (Invitrogen). For the LUMIER-IP and luciferase assays, pcDNA5-FRT-3xFLAG-FFL-Rf (CMV promoter), and L30-HA-RL were used. The cDNAs were of human origin except for mPHAX which was from mouse. For HCT-116 OsTIR1 RPAP3-AID* cell lines all vector maps (repair and guide) can be provided upon request.

Antibodies

Antibodies and dilutions for IF and Duolink were the following: mouse monoclonal anti-RPAP3 at 1:250 dilution (Sigma-Aldrich, SAB1407956); polyclonal rabbit anti-TRBP at 1:100 dilution (Abcam, ab72110); monoclonal mouse anti-Actin at 1:400 dilution (Abcam, ab3280); polyclonal rabbit anti-GAPDH at 1:750 dilution (Abcam, ab9485); monoclonal mouse anti-GAPDH at 1:750 dilution (Abcam, ab8245). Antibodies and dilutions for western blot were the following: rabbit polyclonal anti-RPAP3 at 1:2000 dilution (Sigma-Aldrich, SAB1411438); monoclonal mouse anti-TRBP at 1:500 dilution (Abcam, ab129325); polyclonal rabbit anti-TRBP at 1:500 dilution (Abcam, ab72110); polyclonal rabbit anti-V5 at 1:4000 dilution (ThermoFischer Scientific, GTX117997); antibody for IP was the following monoclonal mouse anti-V5 (ThermoFischer Scientific, 37–7500).

Antibodies for HCT-116 OsTIR1 RPAP3-AID* characterization were the following: polyclonal rabbit anti- tubulin at 1:500 dilution (Sigma, 12G10); polyclonal rabbit anti-HA at 1:1000 dilution (Sigma, H6908); polyclonal rabbit anti-PIH1D1 at dilution 1:500 (PTGLab, 19427–1-AP).

Yeast two-hybrid (Y2H)

For Y2H assays, appropriate pACT2 and pAS2 plasmids were introduced into haploid *Saccharomyces cerevisiae* test strains (Y187 and CG1945, respectively), which were then crossed. Diploids were selected on Leu^-/Trp^- medium and then plated on $Leu^-/Trp^-/His^-$ plates, with 0–40 mM of 3-amino-1,2,4-triazol (3-AT), which is a competitive inhibitor of the product of the HIS3 reporter gene. This was used to evaluate the strength of the interactions. Growth was assessed after three or four days of incubation at 30°C (50).

Co-expression experiments in *Escherichia coli*, protein production and purification

For the TECAN automated screen, *Escherichia coli* BL21 (DE3) pRARE2 cells were co-transformed with the gateway pnEA-3CH and pnCS vectors and growth in Graffinity I buffer (2× LB, 0.5% glucose). Expression was auto-induced by the addition of Graffinity II medium (v/v) (2× LB, 20 mM HEPES (pH7), 0.6% Lactose, 1 mM imidazole) overnight at 20°C, when absorbance reached 1.2 at 600 nm. Purification was performed with His_6-tag Isolation Dynabeads (ThermoFischer Scientific) in low salt (LS: 20 mM Tris-HCl [pH 8], 50 mM NaCl, 7 mM imidazole) or high salt (HS: 20 mM Tris-HCl [pH 8], 500 mM NaCl, 7 mM imidazole) buffers. After three washes with LS or HS buffers, beads were resuspended in 2× Laemmli buffer and loaded on 15% SDS-PAGE or eluted using PreScission (3C) protease overnight on beads at 4°C to remove the N-terminal His_6-tag prior to gel filtration.

For crystallogenesis assays, *E. coli* BL21 (DE3) pRARE2 cells were co-transformed with the pnEA3CH::TRBP (266–366) and pnCS-RPAP3 (133–255) plasmids (40). Cells were grown in LB medium containing 100 μg/ml of ampicillin, 25 μg/ml of chloramphenicol and 25 μg/ml of spectinomycin at 37°C under shaking. Protein expression was then induced with 0.5 mM IPTG for 16 h at 20°C once bacterial culture absorbance was of 0.6–0.8 at 600 nm (A_{600}). Then, the cells were harvested by centrifugation for 30 min at 4000 × *g* at 4°C. The cell pellet was resuspended in 50 ml of purification buffer (25 mM HEPES pH 7.5, 300 mM NaCl, 0.5 mM TCEP, 10 mM Imidazole) and sonicated. The complex was purified using TALON beads (Clontech) after nucleic acid precipitation using 0.05% of PolyEthylImine (PEI) and eluated by using PreScission (3C) protease overnight on beads at 4°C to remove the N-terminal His_6-tag. This step was followed by a preparative gel filtration (HiLoad 16/60 Superdex 75, Cytiva) on an AKTA prime system in 25 mM HEPES buffer (pH 7.5), 300 mM NaCl, 0.5 mM TCEP and 10 mM imidazole. Finally, the complex was concentrated to 11 mg/ml. For co-expression assays, protocol was the same, except we used the gateway version of pnEA-3CH, pnCS and pnYK. Beads were directly resuspended in 2× Laemmli buffer and loaded on 15% SDS-PAGE instead of preparative gel filtration.

GST pull-downs

Total cellular extracts in resuspension buffer (RSB) 100 (100 mM NaCl, 10 mM Tris-HCl pH 7.5, 2.5 mM $MgCl_2$, 0.01% NP40) were pre-cleared on Glutathione Sepharose beads

for 2 h at 4°C. About 4 μg of GST or of the GST-tagged protein of interest attached on Sepharose beads were incubated with 500 μl of pre-cleared cell extract for 2 h at 4°C on a rotating wheel. Beads were washed 5 times in RSB 200 buffer (200 mM NaCl, 10 mM Tris-HCl pH 7.5, 2.5 mM $MgCl_2$, 0.05% NP40). After the last wash, beads were resuspended in SDS-PAGE loading dye and directly submitted to electrophoresis prior western blotting.

PLA and image acquisition

In situ proximity ligation assay (PLA) was performed as recommended by the manufacturer (DuolinkII kit, Olink Bioscience AB). Briefly, HeLa cells grown on coverslips were fixed in 1× PBS, 3% paraformaldehyde during 20 min and permeabilized for 5 min in a 1× PBS, 0.1% Triton X-100 solution. Primary antibodies were diluted in 1× antibody dilution buffer and incubated for 1 h at room temperature. The negative controls used only one of each primary antibody. Cells were washed three times for 5 min in 1× PBS. The PLA probes (Rabbit-MINUS and Mouse-PLUS) were incubated in a pre-heated humidity chamber for 1 h at 37°C. Subsequent steps were performed using the detection reagents green according to DuolinkII kit protocol. Finally, cells were incubated for 20 min with Alexa Fluor™ 546 Phalloidin (Thermo Fischer scientific) to detect the cytoskeleton. The Duolink mounting medium was supplemented with 10 μM TO-PRO-3 final to counterstain nuclei. Laser confocal microscopy was performed with a SP5-AOBS X Leica confocal microscope. Images from each channel were recorded separately and then merged with the ImageJ software.

Co-immunoprecipitation and western blot

Cells are transfected in 10 cm plates with 15 μg of pcDNA3.1/nV5-DEST (Invitrogen) fused with TRBP and 30 μl of JetPEI (Polyplus transfection). After 48 h, cells were lyzed in 500 μl of HNTG buffer (20 mM HEPES, pH 7.9, 150 mM NaCl, 1% Triton X-100, 10% Glycerol, 1 mM $MgCl_2$, 1 mM EGTA) containing protease inhibitor cocktail (Roche) and incubated for 20 min at 4°C. Alternatively, T-Rex stable cell lines were treated with doxycycline to induce expression of the Flag-TRBP or Flag-RPAP3 proteins. Cellular debris were removed by centrifugation for 10 min at 9000 × *g*. Extracts were incubated on G-beads (ThermoFisher Scientific) coupled to 10 μg of anti-V5 or anti-Flag antibodies for 2 h at 4°C. For control IP, beads without antibodies were used. If necessary, extract was incubated with 15 μg of RNAse A (ThermoFisher Scientific). Beads were then washed three times with ice-cold HNTG before being resuspended in 2× Laemmli buffer. Inputs and pellets were loaded on 12% SDS-PAGE and transferred to ethanol-activated PVDF membrane (Protean Amersham). Membranes were blocked with 5% non fat dry milk in PBST (0.1% Tween-20 in PBS) and incubated with V5 or anti-RPAP3 primary antibody diluted in 5% non fat dry milk followed by incubation with secondary antibody conjugated to HRP. Enzymatic activity was detected using the ECL prime kit (Amersham).

Luciferase assays

HEK-293T cells were grown on 96-well plates and co-transfected with 95 ng of plasmid expressing a HA-Tag Renilla Luciferase (RL) in fusion with the protein of interest, and 5 ng of plasmid coding for the Firefly Luciferase alone (FL) with 0.3 μl of JetPrime (Ozyme). After 48 h, cells were extracted in 50 μl of ice-cold 1× HNTG buffer containing protease inhibitor cocktail (Roche) and incubated at 4°C for 15 min. RL and FL activities were measured on 96-well plates using 2 μl of cell extract containing 8 μl of 1× PLB (Promega) and the Dual Luciferase Assay Kit (Promega). Values obtained for RL were normalized to FL values. Experiments were done at least in triplicate. For geldanamycin (GA) experiments, drug was added 16 h before extraction to a final concentration of 2 μM.

LUMIER IP

HEK-293T cells were grown in 24-well plates and co-transfected with 450 ng of the RL fusion and 50 ng of the 3× FLAG-FL fusion. After 48 h, cells were extracted in 500 μl of ice-cold HNTG containing protease inhibitor cocktail (Roche), incubated for 15 min at 4°C and spun down at 4°C at 20 000 × *g* for 15 min. 100 μl of the extract were dispatched in two wells in a 96-well plate, with one well being coated with anti-FLAG antibody (10 μg/ml in 1× PBS, F1804 Sigma Aldrich), and one control well without antibodies. Plates were incubated for 3 h at 4°C, and then washed 5 times with 300 μl of ice-cold HNTG, for 10 min at 4°C for each wash. After the last wash, 10 μl of 1× PLB (Promega) was added in each well. To measure the input, 2 μl of extract and 8 μl of 1× PLB were mixed in new wells. Plates were then incubated for 5 min at room temperature, and FL and RL Luciferase activities were measured in IP and input wells, using the Dual Luciferase Kit (Promega). Experiments were done at least in triplicate. Co-IP efficiency was defined as the RL/FL ratio in the pellet, divided by the RL/FL ratio in the input. Unless stated otherwise, statistical significance was evaluated using *Z*-test assaying whether the co-IP efficiency in the anti-FLAG IP was >11 times higher than the mean values obtained in the control IP, done without antibodies.

Let-7 reporter assay

HCT-116 OsTIR1 WT cells and HCT-116 ostir1 RPAP3-AID* were grown in 24-well plates and treated 24 h later with 500 μM of IAA 6 h prior to co-transfection with 50 ng of pRL-3xBulge (51) (Let7 WT) or pRL-3xBulgeMut (Let7 Mut), 50 ng of FL and 400 ng of L30 Myc PHAX as DNA carrier. After 48 h, cells were extracted in 500 μl of ice-cold 1× HNTG containing protease inhibitor cocktail (Roche), incubated for 15 min at 4°C and spun down at 4°C at 20 000 × *g* for 15 min. Cells were next frozen at −20°C. RL and FL activities were measured in 96-well plates using 2 μl of cell extract containing 8 μl of 1× PLB (Promega) using the Dual Luciferase Assay Kit (Promega) (52). Values obtained for RL were normalized to FL values. Experiments were done in triplicate.

Stem-loop RT-qPCR

Total RNAs were extracted using TRIzol and were quantified using a nanodrop 2000. DNase step was performed on 1 μg of RNA for 30 min at 37°C using RQ1 DNase in a 10 μl final volume. The reaction was stopped by adding 1 μl of RQ1 stop buffer for 5 min at 65°C. Then, 20 or 200 ng of RNA were reverse transcribed using the Taqman miRNA Reverse Transcription Kit (ThermoFischer reference 000377) or using the pri-miRNA kit (ThermoFischer reference Hs03302533), respectively. cDNAs were diluted two times in water and RNA expression level was assessed by real time quantitative PCR (RT-qPCR) using the corresponding Taqman probes and ViiA-7 Real-Time PCR system (Applied Biosystems). RNA levels were normalized against U6 snRNA as a reference gene (ThermoFischer reference 001973), and fold change expression of mature Let7 and pri-Let7 after RPAP3 depletion were calculated using the $\Delta\Delta C_T$ method.

Nuclear magnetic resonance

A perdeuterated $^{13}C/^{15}N$ labeled sample of the complex between RPAP3-TPR1 (i.e. fragment 133–155 of human RPAP3) and TRBP-dsRBD3 (i.e. fragment 262–366 of human TRBP) was prepared as the X-ray sample, except that bacteria were initially grown in a minimal M9 medium supplemented with ^{13}C-D6-glucose, ^{15}N ammonium chloride and 50% D_2O. The final sample was concentrated at 1 mM in 10 mM NaPi, 150 mM NaCl, 5 mM ^2H DTT and is stable for about 2 days.

^1H-^{15}N HSQC, HNCO, HNCA, HNCACB, CBCACONH and a ^1H-^{15}N NOESY-HSQC (with a mixing time of 120 ms) spectra were recorded at 303 K on 600 and 950 MHz spectrometers equipped with cryoprobes. Assignment of backbone resonances was performed with CARA (53). The chemical shift data were derived into secondary structures using TALOS+ (54). Free and TRBP-dsRBD3 bound states of RPAP3-TRP1 were compared using a previous assignment performed in the same experimental conditions (BMRB entry19758, (42) and a composite ^1H-^{15}N chemical shift calculated for each residue as follow: $\Delta\delta = \sqrt{(\delta^1 H_{free} - \delta^1 H_{bound})^2 + 0.1(\delta^{15} N_{free} - \delta^{15} N_{bound})^2}$. The assignment of the free RPAP3-TPR1 was obtained using a protein fragment holding four non-native residues located at its N-terminal position. To avoid a bias on chemical shift perturbations generated by this difference in the primary structure, residues in proximity of the N-terminal tail of RPAP3-TPR1 were discarded from the analysis. The residues in RPAP3-TPR1 with a Δδ value superior to the centile 80 value were considered as significantly perturbed upon binding of TRBP-dsRBD3.

Protein crystallization, X-ray data collection and structure determination

Crystallization and X-ray data collection. Crystals of the complex between RPAP3 (residues 133–255) and TRBP (residues 262–366) were grown by vapor diffusion in hanging drops. Drops were made at 293 K by mixing 2 μl of the protein solution at 11 mg/ml and 2 μl of a reservoir solution containing 18% (w/v) PEG 3,350 and 8% (v/v) Tacsimate™ at pH 6.0. Crystals belong to space group $P2_12_12$ with unit-cell parameters $a = 39.8$ Å, $b = 158.1$ Å and $c = 32.7$ Å. Assuming one heterodimer in the asymmetric unit, the packing density V_M is 2.00 Å^3.Da^{-1} and the solvent content is 38.4%. Crystals were flash frozen in liquid nitrogen in the mother liquor with addition of 25% glycerol as cryoprotectant. A native data set at 1.49 Å resolution was collected at 100 K on beamline ID29 at the European Synchrotron Radiation Facility (ESRF, Grenoble), with incident radiation at a wavelength of 1.033 Å and a crystal-to-detector distance of 207 mm. Diffraction spots were recorded on a Pilatus 6M-F detector with a 0.1° oscillation and a 0.04 second exposure per image. Data were indexed and scaled using XDS (55) and indexed intensities were converted to structure factors using TRUNCATE in the CCP4 suite (56) without any σ cut-off.

Table 1. Crystallographic data collection and refinement statistics.

Data collection	
Space group	$P2_12_12$
Cell parameters	$a = 39.8$ Å, $b = 158.1$ Å, $c = 32.7$ Å
Wavelength (Å)	1.033
Resolution (Å)	50.0–1.49
R_{sym} (%)[a,b]	5.9 (27.9)
Completeness (%)[a]	99.0 (94.1)
$<I/\sigma(I)>$[a]	18.6 (5.1)
Multiplicity[a]	6.2 (6.3)
Refinement	
Resolution (Å)	40.0–1.49
No. reflections	31848
No. free reflections	1353
R_{factor}(%)[c]	17.8
R_{free} (%)[d]	21.1
r.m.s.d. Bonds (Å)	0.021
r.m.s.d. Angles (°)	2.054
Mean B value (Å^2)	16.1
No. of protein atoms	1701

[a]Number in parentheses corresponds to the last resolution shell 1.49–1.59 Å.
[b]$R_{sym} = \Sigma|I-<I>|/\Sigma I$
[c]$R_{factor} = \Sigma||F_{obs}|- |F_{calc}||/\Sigma|F_{obs}|$
[d]For R_{free} calculation, 4% of data were selected.

Crystal structure determination. The crystal structure of the RPAP3:TRBP complex was solved by molecular replacement with the program PHASER (57) using the coordinates of RPAP3 from the crystal structure of RPAP3 bound to a HSP90 peptide ((38); PDB 4CGV) and the coordinates of TRBP bound to Dicer ((10); PDB 4WYQ). A single solution was obtained with LLG = 795 and TFZ = 18.2. Building of the model was performed using Coot (58), and the refinement of the crystal structure was performed in the range 40–1.49 Å using REFMAC5 (59). A total of 4% of the native data were selected for R_{free} calculations. The model was refined to the final R_{factor} of 17.8% and R_{free} of 21.1% (Table 1) and includes residues 133–249 of RPAP3, residues 263–365 of TRBP and 243 water molecules. Because of the lack of density, residues 250–265 of RPAP3 and residues 262 and 366 of TRBP were not built. They were probably too flexible in the complex to generate a clear electron density. Coordinates of the RPAP3:TRBP structure have been deposited in the Protein Data Bank (acces-

sion number 6ZBK). Over 97% of the residues were within the most favored regions, and no residue was within the disallowed regions in a Ramachandran plot, as defined by PROCHECK (60). Averaged *B* factors were of 15.3 Å^2 for the protein atoms, 26.5 Å^2 for water molecules and 16.7 Å^2 for the whole structure. Figures were prepared using PyMOL (The PyMOL Molecular Graphics System, Version 1.8 Schrödinger, LLC).

RESULTS

Human TRBP interacts with RPAP3 *in vitro* and in human cells

To determine whether the R2TP complex might be linked to miRNP or RISC assembly, and to identify putatively novel protein/protein interactions between co-chaperones and components of the miRNA biogenesis machinery, we performed a candidate-based yeast two-hybrid (Y2H) screen in *S. cerevisiae*. Interestingly, we found that RPAP3, a member of the R2TP complex, efficiently associated with TRBP, one of the two cofactors of Dicer (Figure 1A, left and middle panels, Supplementary Figure S1a,b) (12), but not with PACT, despite a similar overall structural organization (Figure 1A, right panel, Supplementary Figure S1 b–f). The association between RPAP3 and TRBP appeared rather strong, as diploid cells grew at a concentration of 3-AT up to 40 mM, which is comparable to the positive control association between Dicer and TRBP (Figure 1A, left and middle panels). As interactions detected by Y2H assays might be mediated by additional factors, we performed co-expression and co-purification experiments in *E. coli* to test whether the TRBP:RPAP3 interaction was direct (Figure 1B, Supplementary Figure S2 a,b). At low salt conditions (50 mM NaCl), RPAP3 co-purified with a His_6-tagged version of TRBP on TALON cobalt beads (Figure 1B, LS). Additionally, using *in vitro* assays with purified recombinant proteins and purification on glutathione beads, the His_6-tagged TRBP protein co-purified with GST (glutathione-S-transferase)-tagged RPAP3, but not with GST alone (Supplementary Figure S3a, compare lanes 4 and 3). Because we validated these interactions using recombinant proteins expressed in *E. coli*, we additionally validated the interaction between RPAP3 and TRBP by co-immunoprecipitation in human embryonic kidney cells. We observed that TRBP and RPAP3 co-immunoprecipitated using a doxycycline inducible HEK293 T-Rex cell line endogenously expressing a flagged-RPAP3 (Figure 1C, lane 6), as well as using a transiently expressed V5 tagged-TRBP, even in cell lysates treated with RNase A, suggesting that the interaction was not mediated by RNA (Supplementary Figure S3b, lanes 2 and 4, respectively). Finally, we validated the interaction of both endogenous TRBP and RPAP3 *in cellulo* using a proximity ligation (Duolink) assay in HeLa cells (Figure 1D, RPAP3:TRBP/PLA and merge; Supplementary Figure S3c). Based on the overall data, we concluded that RPAP3 directly interacts with TRBP, both *in vitro* and *in cellulo*.

The TPR1 domain of RPAP3 binds the non-canonical type B dsRBD (dsRBD3) of TRBP

To define the domain of RPAP3 that mediates the interaction with TRBP, we performed co-expression and co-purification experiments in *E. coli* and Y2H assays in *S. cerevisiae*, using different protein sub-domains (61,62) (Figure 2 and Supplementary Figure S4). In metazoan, RPAP3 contains two tetratricopeptide (TPR) domains, each composed of 3 TPR motifs and a capping helix at the C-terminal end (42,63) (Figure 2A). Two highly soluble TPR domains have been defined in RPAP3, the TPR1 encompassing residues 133 to 255 and the TPR2 including residues 281 to 396. On the other hand, TRBP folds into 3 evolutionary conserved dsRBDs (11). The two N-terminal ones mediate dsRNAs binding (residues 18–99 and 157–228, respectively (64,65), while the C-terminal one mediates the interaction with Dicer (residues 262–366; Figure 2A). By using co-expression and co-purification assays (Figure 2B) and yeast two-hybrid assays (Figure 2C, left panel, Supplementary Figure S4a), we found that the TPR1 domain of RPAP3 is both necessary and sufficient for TRBP binding (lanes c, g, i, m and o in Figure 2B; RPAP3 133–255 in Figure 2C). Surprisingly, this is not the case for the TPR2 domain, despite its strong homology with the TPR1 (lanes q, r, s and t in Figure 2B; RPAP3 281–396 in Figure 2C). Noticeably, interactions were always detected only in low salt condition and some interactions were not detected when His_6-tag was fused to the second partner (lanes a, b, e; f, k and l in Figure 2B). Next, we used a similar strategy to define the region of TRBP required for RPAP3 binding. We found that the dsRBD3 domain (262–366) of TRBP (Figure 2D right panel, Supplementary Figure S4b), but not the dsRBD1 and dsRBD2 domains (Figure 2D, left and middle panels, Supplementary Figure S4 b), interacted with the TPR1 domain of RPAP3, which was confirmed using Y2H assay (Figure 2C right, Supplementary Figure S4a).

Finally, to define more precisely the RPAP3-binding site in the TRBP dsRBD3, we performed similar experiments with shorter TRBP fragments (Supplementary Figure S4c). Collectively, these experiments revealed that the TRBP dsRBD3 C-terminal part, residues 293–366, was sufficient for RPAP3 binding. We concluded that the RPAP3 TPR1 domain interacts directly with the TRBP dsRBD3, and more precisely with its region spanning amino acids 293–366.

The TRBP:RPAP3 and the TRBP:Dicer interactions are mutually exclusive

The dsRBD3 domain of TRBP was shown to be the domain involved in the interaction with Dicer (10,11,64,66). Therefore, to assess whether a ternary complex containing Dicer, TRBP and RPAP3 could be formed, we performed simultaneous co-expression experiments in *E. coli* of the three protein minimal subdomains involved in the respective interactions (Figure 3). We found that both the TPR1 domain of RPAP3 and the 256–595 domain of Dicer co-purified with a His_6-tagged version of TRBP dsRBD3 on TALON® beads (Figure 3A, beads). However, when the eluate was loaded onto a gel filtration column, the elution profile clearly showed two distinct peaks corresponding to TRBP:RPAP3 and TRBP:Dicer sub-complexes, respectively (Figure 3B,C, Supplementary Figure S4d). This indicated that the dsRBD3 of TRBP could not interact simultaneously with Dicer and RPAP3, probably due to steric constrains as the same domain of TRBP seems to be in-

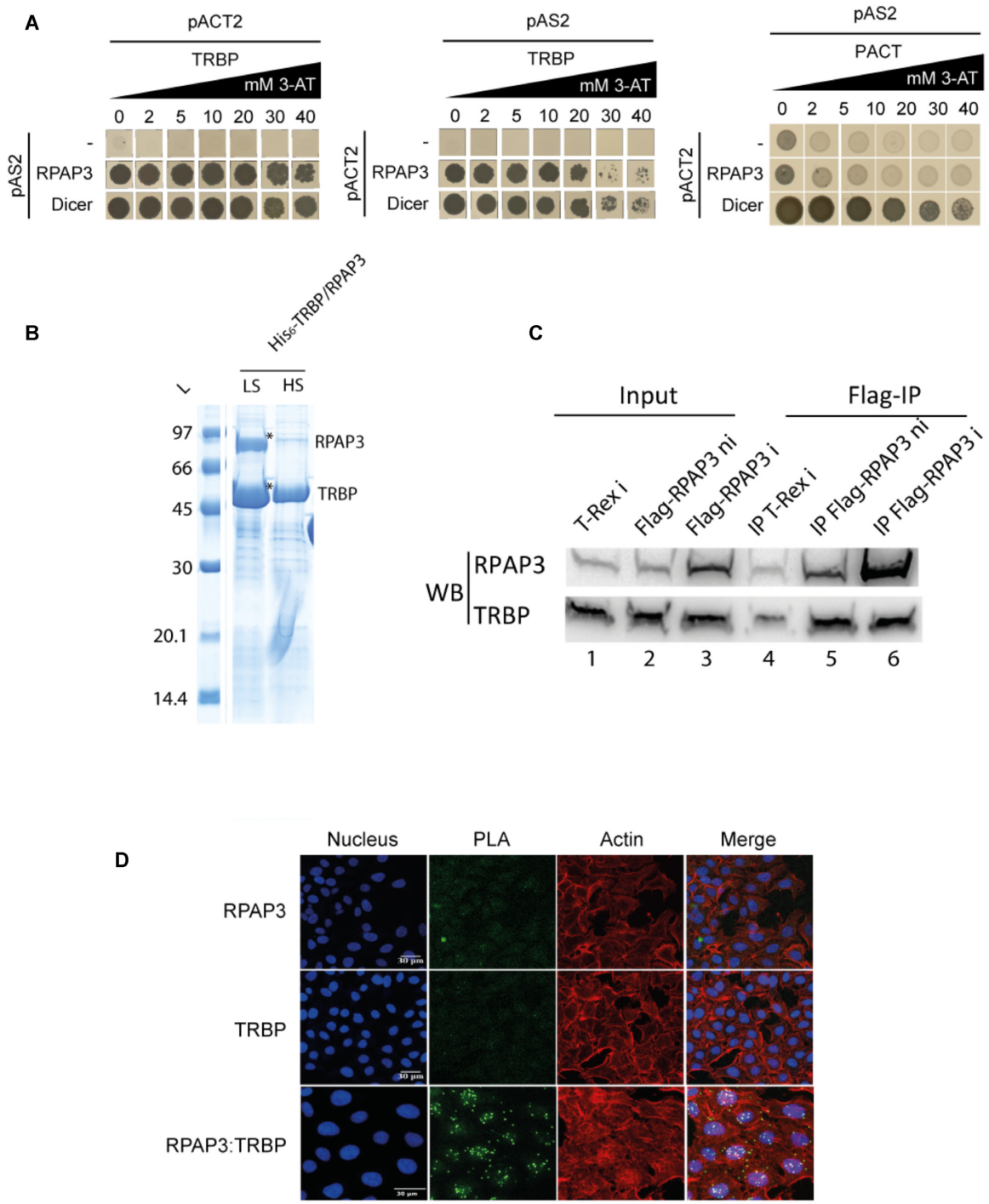

Figure 1. Characterization of the TRBP:RPAP3 interaction. (**A**) A candidate-based yeast two-hybrid (Y2H) screen performed in the yeast *Saccharomyces cerevisiae* revealed an association between TRBP and RPAP3 in both orientations (left and middle panels). On the contrary, RPAP3 does not bind to PACT (right panel). The TRBP:Dicer interaction was used as a positive control. pAS2 and pACT2 plasmids expressed a protein fusion with the DNA binding domain or activation domain of transcription factor Gal4, respectively. The strength of the interactions was tested using increasing amounts of 3-amino-triazol (3-AT) from 0 to 40 mM. (**B**) Co-expression and co-purification experiments in *Escherichia coli.* RPAP3 co-purified with a hexa-histidine His_6-tagged version of TRBP on cobalt-based immobilized metal affinity chromatography (IMAC*)* beads (TALON) at low salt concentration (LS, 50 mM NaCl), but not in high-salt conditions (HS, 500 mM NaCl). Individual protein expression control experiments for both untagged TRBP or RPAP3 proteins are shown in Supplementary Figure S2a. (**C**) Co-immunoprecipitation experiments performed in the T-Rex HEK293 cell line expressing a flagged version of RPAP3 upon doxycycline induction. ni: no doxycycline induction, i: doxycycline induction. Western blot reveals that TRBP is co-immunoprecipitated with the flagged RPAP3 protein (lane 6). Leaks of the tetracycline repressor system enable some immunoprecipitation of TRBP also in the not induced control (lane 5) but not in the control without flagged RPAP3 (lane 4). (**D**). *In cellulo* Duolink assays performed in HeLa cells. Proximity ligation assay (PLA) reveals a close proximity of the endogenous TRBP and RPAP3 proteins in favor of their direct interaction, as each dot in the RPAP3:TRBP/PLA or merge reveals a RPAP3:TRBP association. Nuclei were stained using DAPI, and cytoplasmatic actin using Alexa Fluor 546. Scale bar is 30 μm. See Materials and Methods for details.

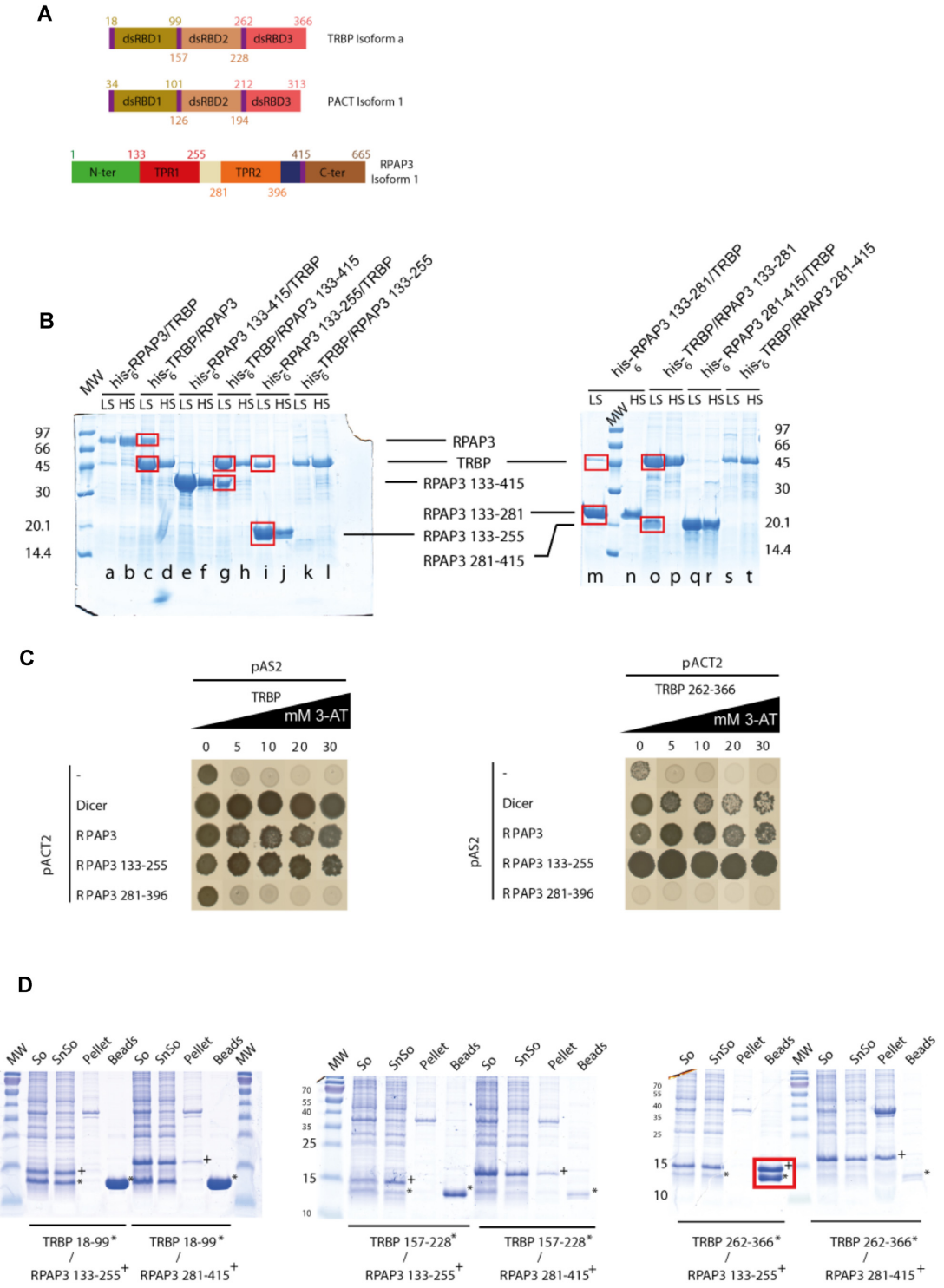

Figure 2. Identification of the protein subdomains involved in the interaction. (**A**) Representation of the subdomains of TRBP and RPAP3 as predicted with the software IUPRED and PSIPRED (61,62). Numbers correspond to the amino acid residues located at each domain extremities. (**B**) Co-expression and co-purification experiments in *E. coli* performed with RPAP3, TRBP and their subdomains. For each protein pair, the first protein name on top of the gel always indicates the His6-tagged protein. The beads were directly resuspended in 2x Laemmli buffer and fractionated on 15% SDS-PAGE. Positive interactions are highlighted with red squares. (**C**) Two-hybrid screens performed in the yeast *S. cerevisiae* on TRBP, RPAP3 and their subdomains. The TRBP:Dicer interaction was used as a positive control. pAS2 and pACT2 plasmids respectively enable expression of a protein fusion with the DNA binding domain or activation domain of transcription factor Gal4. Strengths of the interactions were tested using increasing amounts of 3-amino-triazol (3-AT) from 0 to 30 mM. (**D**) Purification steps of co-expression experiments in *E. coli* performed with RPAP3 (*) and TRBP (+) subdomains and analyzed by SDS-PAGE. The TRBP and RPAP3 domains used are indicated below the gel lanes. The TRBP subdomains carried the His6-tag. 'So', 'SnSo', 'Beads', 'MW' and 'Pellet' design respectively the culture sonicate, supernatant sonicate, Talon beads, Molecular Weight marker and sonicate pellet. The positive interaction (dsRDB3 of TRBP and TPR1 of RPAP3) is highlighted with a red square. None of the TRBP domains interacted with the TPR2 of RPAP3.

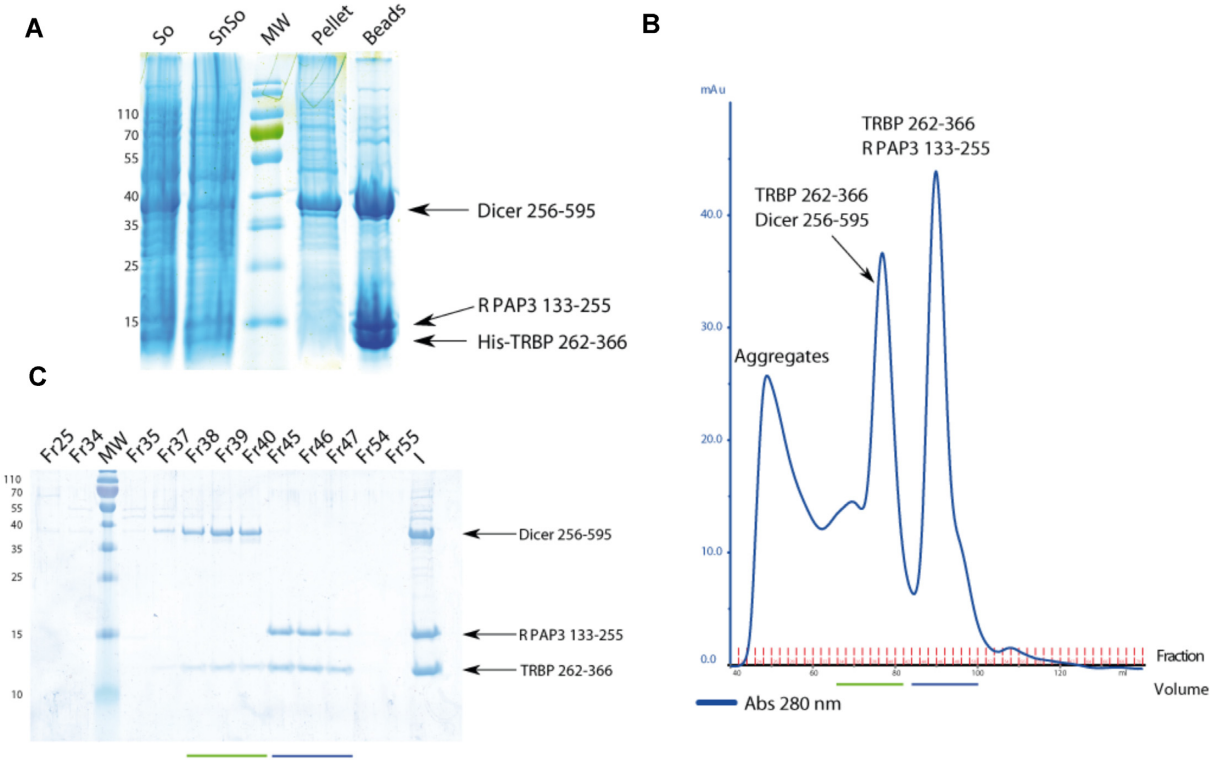

Figure 3. The same binding surface of TRBP seems to be involved for its interactions with Dicer or RPAP3. (**A**) Co-expression and co-purification steps experiments in *E. coli* of the three minimal protein subdomains (indicated on the right of the SDS-PAGE gel, His6-tag on TRBP) involved in the TRBP:RPAP3 and TRBP:Dicer interactions as determined in our study. The Dicer subdomain used (256-59) contains the partner binding domain and is involved in the interaction with TRBP (10). 'So', 'SnSo', 'Beads', 'MW' and 'Pellet' relate respectively to the culture sonicate, supernatant sonicate, Talon beads, molecular weight markers and sonicate pellet. (**B**). Elution profile of the gel filtration assay performed on the 3 co-expressed TRBP, RPAP3 and TRBP minimal subdomains. (**C**). Fractions collected were loaded onto a 10% SDS-PAGE. Distinct complexes are underlined in green and blue in (B) and (C).

volved in both interactions. Interestingly, a major part of TRBP is found with RPAP3 in the main peak and only a minor part with Dicer. This could suggest that the affinity of the dsRBD3 of TRBP is higher to RPAP3 than for Dicer.

Structure of the human RPAP3:TRBP complex

In order to highlight the structural features of the interaction between the TPR1 domain of RPAP3 and the dsRBD3 of TRBP, we crystallized the heterodimer and collected X-ray diffraction data at 1.49 Å resolution (Figure 4 and Table 1; see Materials and Methods). The RPAP3 core (residues 133–249) consists of seven α-helices arranged in a repeating antiparallel right-handed helix topology and was already described as a TPR (tetratricopeptide repeat) domain in the crystal structure of RPAP3 bound to the C-terminal tail peptide (SRMEEVD) of HSP90 (38,40,42) (Supplementary Figure S5a, in blue). On the other hand, the TRBP structure (residues 262–366) contains a α/β sandwich (residues 289–366) typical of a dsRBD fold (Supplementary Figure S5b, in purple), with three β-strands (β1, β2, and β3) and two α-helices (H4 and H5), as already described (10). Interestingly, the crystal structure of RPAP3 (residues 133–249) bound to TRBP is similar to that of RPAP3 bound to the C-terminal tail peptide (SRMEEVD) of HSP90 (38,40,42), Supplementary Figure S5a, in green. Similarly, the dsRBD core of TRBP bound to RPAP3 is structurally similar to the dsRBD domain of TRBP in complex with Dicer (10) (Supplementary Figure S5b, in orange). These observations suggest that no significant conformational modification occurs on neither protein upon binding to each other. Interestingly, however, an N-terminal extension (residues 262–288) beyond the canonical dsRBD domain of TRBP is observed in the crystal structure of the RPAP3:TRBP complex and consists of 3 helices H1, H2 and H3 (Supplementary Figure S5b, in orange, and Supplementary Figure S5 c). This N-terminal extension was shown to be partially disordered in the crystal structure of TRBP bound to Dicer (10) (see supplementary materials for a detailed structural description).

As suspected from our co-expression and gel filtration experimental results (Figure 3), the crystal structure revealed that the protein interface involves the second α-helix H5 as well as β-strands β2 and β3 of the dsRBD3 of TRBP (Figure 4A). We confirmed these data using solution-state NMR spectroscopy. We assigned backbone resonances of the RPAP3-TPR1:TRPB-dsRBD3 complex and, thanks to TALOS-N calculations, we showed that the two partners fold similarly in solution and in the crystal (Supplementary Figure S6). Then, we measured chemical shift perturbations of backbone amide groups in RPAP3-TPR1 upon binding

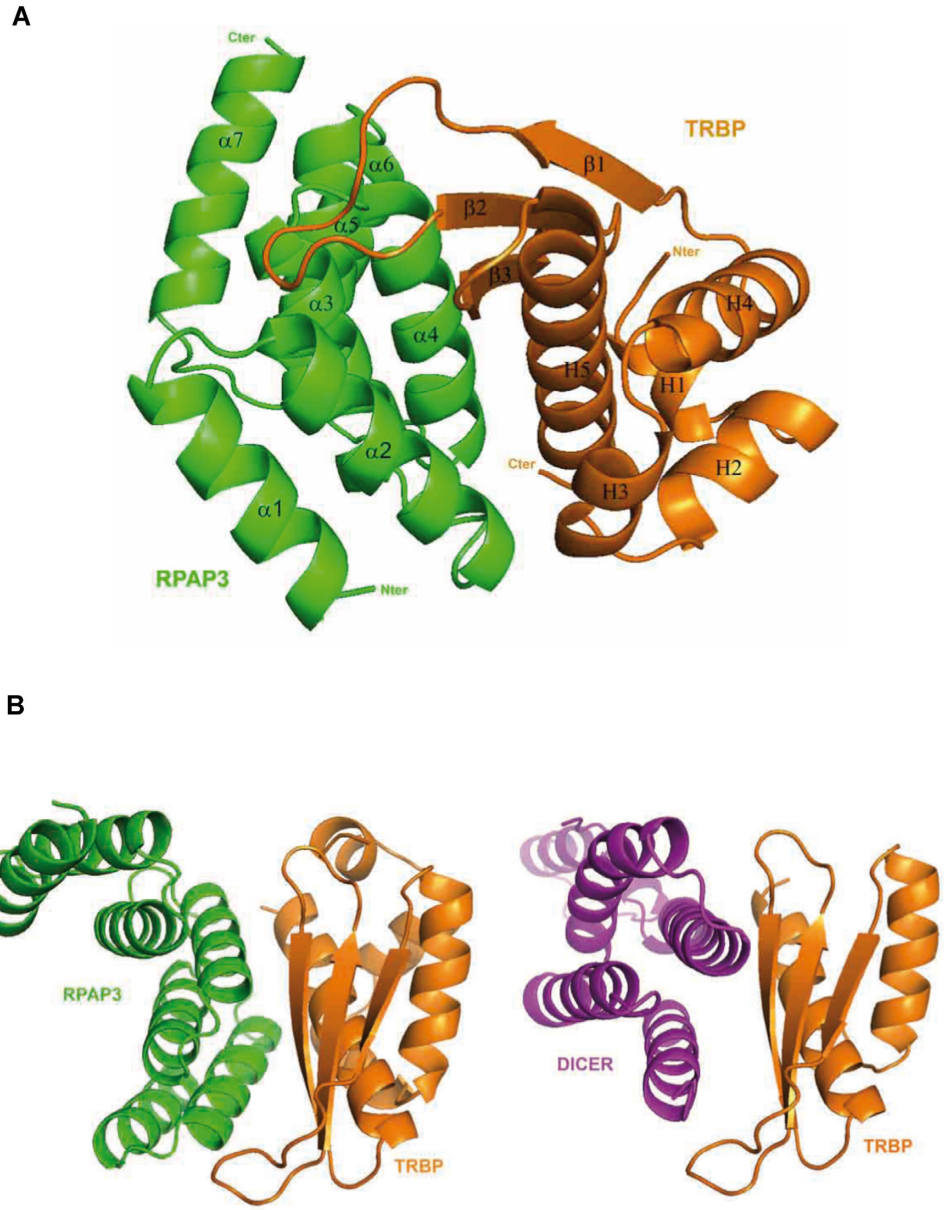

Figure 4. Crystal structures of the TRBP:RPAP3 complex. (**A**) Ribbon representation of the X-ray crystallographic structure of the TPR1 domain of RPAP3 and the dsRBD3 of TRBP at 1.49 Å resolution. RPAP3 (residues 133–249) and TRBP (residues 263–365) are drawn in green and orange, respectively. (**B**) Ribbon representations of our crystal structure (left) and the one published by Wilson *et al.* (10) (right) confirm that TRBP shares the same binding interface for its interaction with either Dicer or RPAP3.

of TRBP-dsRBD3 (Figure 5A,B). This NMR mapping revealed that major perturbations are observed in helices α2 and α4 of RPAP3-TPR1, in accordance with the binding interface observed in the X-ray structure. Since these helices are also involved in the interaction with Dicer (10), this confirmed that the TRBP interaction with RPAP3 or Dicer are mutually exclusive in solution, even if Dicer and RPAP3 do not share any overall structure similarities (Figure 4B).

In contrast, binding of RPAP3 to TRBP involves the convex surface, i.e., the opposite face of the TPR domain compared to that involved in HSP90 binding, suggesting that HSP90 binding should not be altered by TRBP binding (a detailed structural description is available in the Supplementary Materials section). Superimposition of the RPAP3:TRBP structure with the structure of RPAP3 (TPR1) bound to the C-terminal tail peptide (SRMEEVD) of HSP90 (38,40) indeed shows that the RPAP3 surface binding to the HSP90-tail peptide is far away from the RPAP3:TRBP interface (Figure 5C). We hypothesized that binding of TRBP to RPAP3 should not prevent the recruitment of HSP90 and HSP70 by the R2TP complex. Co-expression and co-purification experiments in *E. coli* of different domains of RPAP3, TRBP (262–366) and HSP70/90 revealed co-elution of the 3 partners (Figure 5D).

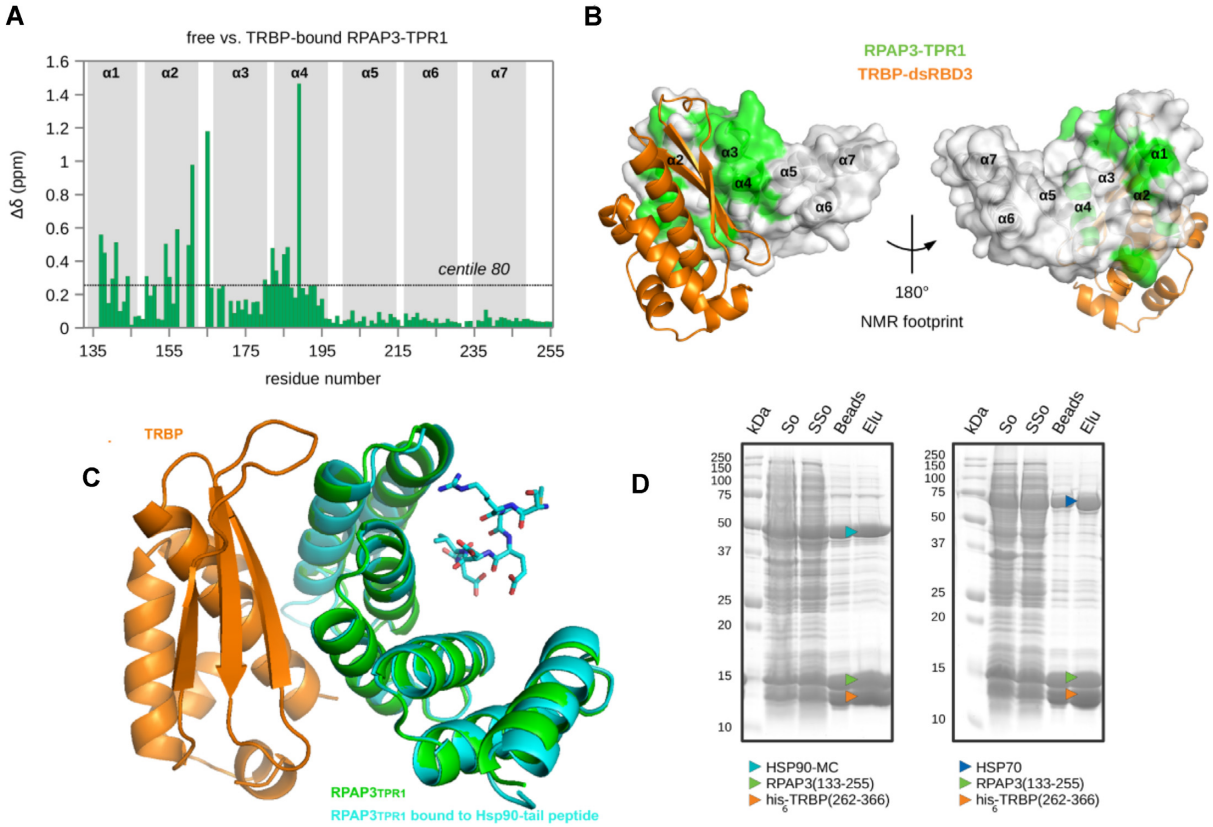

Figure 5. Two distinct surfaces of RPAP3 bind TRBP and the HSP90-tail peptide. (**A**) Chemical shift perturbations of RPAP3-TPR1 upon binding of TRBP-dsRBD3. Backbone amide group resonances of the free and TRPB bound-states of RPAP3-TPR1 were compared using composite 1H-15N chemical shifts (Δδ). Data were plotted againt the sequence of RPAP3. Position of helices was indicated in gray and the value corresponding to centile 80 was indicated with a dotted line. (**B**) Residues in RPAP3 for which the Δδ value was superior to the centile 80 value were reported in green on the molecular surface of RPAP3-TPR1. The X-ray structure of the RPAP3-TPR1 (133–255):TRBP-dsRBD3 (262–366) complex was used. (**C**) Superimposition of the crystal structure of RPAP3-TRBP (in green and orange) with the crystal structure of RPAP3 bound to the HSP90-tail peptide (in cyan) (38) (PDB 4CGV). The HSP90-tail peptide (SRMEEVD) is shown as sticks. (**D**) The RPAP3-TPR1:TRBP-dsRBD3 complex co-elutes with HSPs. Protein co-expression assays in *E. coli* with the His6-TRBP-RPAP3 complex and human HSP70 or HSP90-MC. 'So', 'SSo', 'Beads' and 'Elu' relate respectively to the culture sonicate, supernatant sonicate, Talon beads and elution from the beads with imidazole. The co-purified proteins are indicated with colored arrows.

Identification of key residues involved in the interaction between RPAP3 and TRBP

Based on the crystal structure of the interface between human TRBP and RPAP3, we performed a mutational analysis and tested the TRBP:RPAP3 interaction by co-expression and co-purification experiments in *E. coli* and co-immunoprecipitation assays. We substituted several residues within the TPR1 domain of RPAP3 with alanine (Supplementary Table S1). Some of the mutated proteins, e.g. RPAP3 L192A (Supplementary Figure S7a), were expressed at low levels in *E. coli,* suggesting that the mutations affected the folding and/or stability/solubility of the protein (data not shown). Then, by inspection of the conserved inter-protein polar contacts involving side chains, we identified three possible important intermolecular interactions in the RPAP3:TRBP complex, namely residues D150 (RPAP3) with S320 (TRBP), T157 (RPAP3) with R354 (TRBP) and D161 (RPAP3) with Q357 (TRBP) (hydrogen bonds) (Figure 6 and Supplementary Figure S7). In agreement with these structural data, individual mutations of all these residues except for S320A (TRBP)/D150A (RPAP3) (Supplementary Figure S7b), destabilized the RPAP3:TRBP interaction. Interestingly, the point mutation V185A on RPAP3 had a drastic effect on TRBP binding without affecting protein solubility, showing that this residue is crucial for the interaction as assumed from the structure of the complex (Supplementary Figure S7c). Next, we tested the interactions in human cells using IP-LUMIER experiments. The mutation of D161A on RPAP3, which was found hydrogen bonded to Q357 in TRBP, disrupted the complex (Figure 6A). This pair of residues was particularly interesting as mutant Q357A in TRBP also disrupted its interaction with RPAP3, but not with Dicer, as revealed by IP-LUMIER experiments (Figure 6B,C), while TRBP mutant R354E failed to interact both with RPAP3 and Dicer (data not shown). This mutagenesis analysis thus identifies a residue of TRBP whose mutation selectively affects binding to RPAP3 but not Dicer. Interestingly, this D161 amino acid is substituted by A310 in the TPR2 of RPAP3, which could explain why TRBP does not bind this second TPR domain.

TRBP, Dicer and AGOs require HSP90 activity

We showed that TRBP, RPAP3 and HSP90 co-eluted after co-expression and co-purification experiments (Figure 5).

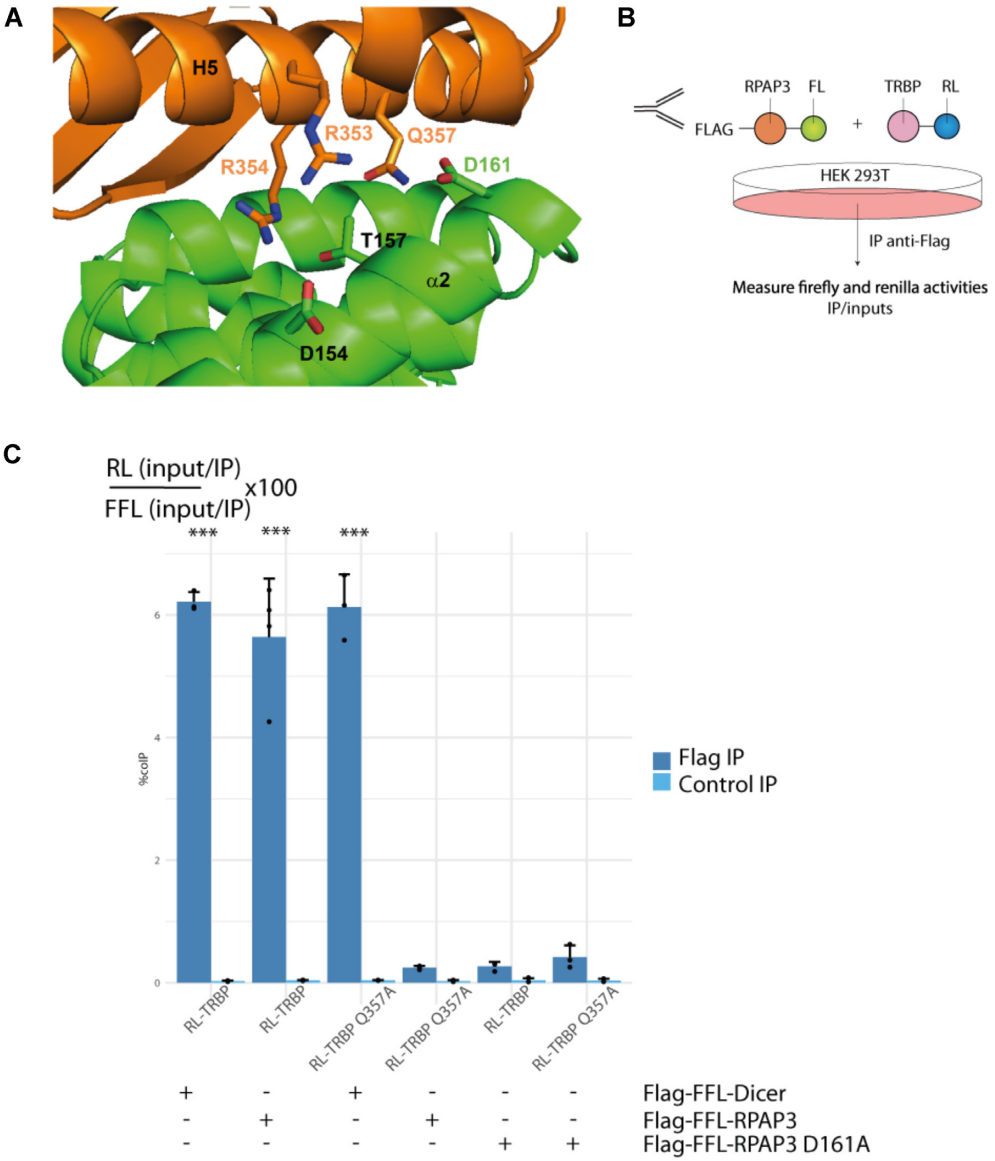

Figure 6. Identification of key residues involved in TRBP:RPAP3 binding interface. (**A**) Network of ionic interactions as well as hydrogen bonds between RPAP3 and TRBP. RPAP3 and TRBP are drawn in green and orange, respectively. (**B**) Principle of the LUMIER-IP test. (**C**) Bar plot showing LUMIER-IP co-efficiency for the interaction of Dicer, RPAP3 or RPAP3 mutant D161A with TRBP WT or TRBP mutant Q357A. *** *P*-value < 0.001 (*Z*-test comparing values of the FLAG IPs with eleven times the mean value obtained in the control IP).

In order to investigate the possible involvement of the entire R2TP complex rather than RPAP3 alone, we verified whether TRBP was able to co-precipitate R2TP core proteins other than RPAP3, using a transiently expressed V5 tagged-TRBP. We observed that all the R2TP proteins, namely PIH1D1 and RUVBL1/2 were efficiently co-precipitated by V5-TRBP (Figure 7A, lane 4, V5) and not in the control without antibody (Figure 7A, lane 4, CT), whereas we did not detect TRBP interactions with PIH1D1 or the RUVBL1/2 proteins in our initial candidate-based yeast two-hybrid screen. This may be explained by an indirect interaction mediated by RPAP3, and indeed most interactions were lost when we used TRBP mutant R354E, defective for RPAP3 binding (Figure 7A, lane 6). However, even when the interaction with RPAP3 was not detectable, TRBP could still co-precipitate RUVBL2 (Figure 7A, lane 6, V5), indicating a possible direct connection between TRBP and RUVBL2.

Finally, in order to determine whether TRBP, Dicer or AGO1/2 proteins could be clients of the HSP90/R2TP chaperoning system, we tested their stability after HSP90 inhibition with Geldanamycin, a drug often leading to HSP90 client destabilization (24,28). To this end, we transfected plasmids expressing each of these proteins fused to the Renilla Luciferase (RL) together with a Firefly Luciferase (FL) control vector (Figure 7B). Remarkably, with the exception of Renilla Luciferase and two unrelated control proteins mPHAX and CSRP2 (67,68), all proteins were sensitive to Geldanamycin, revealing the importance of HSP90 for their stability, as was previously shown for

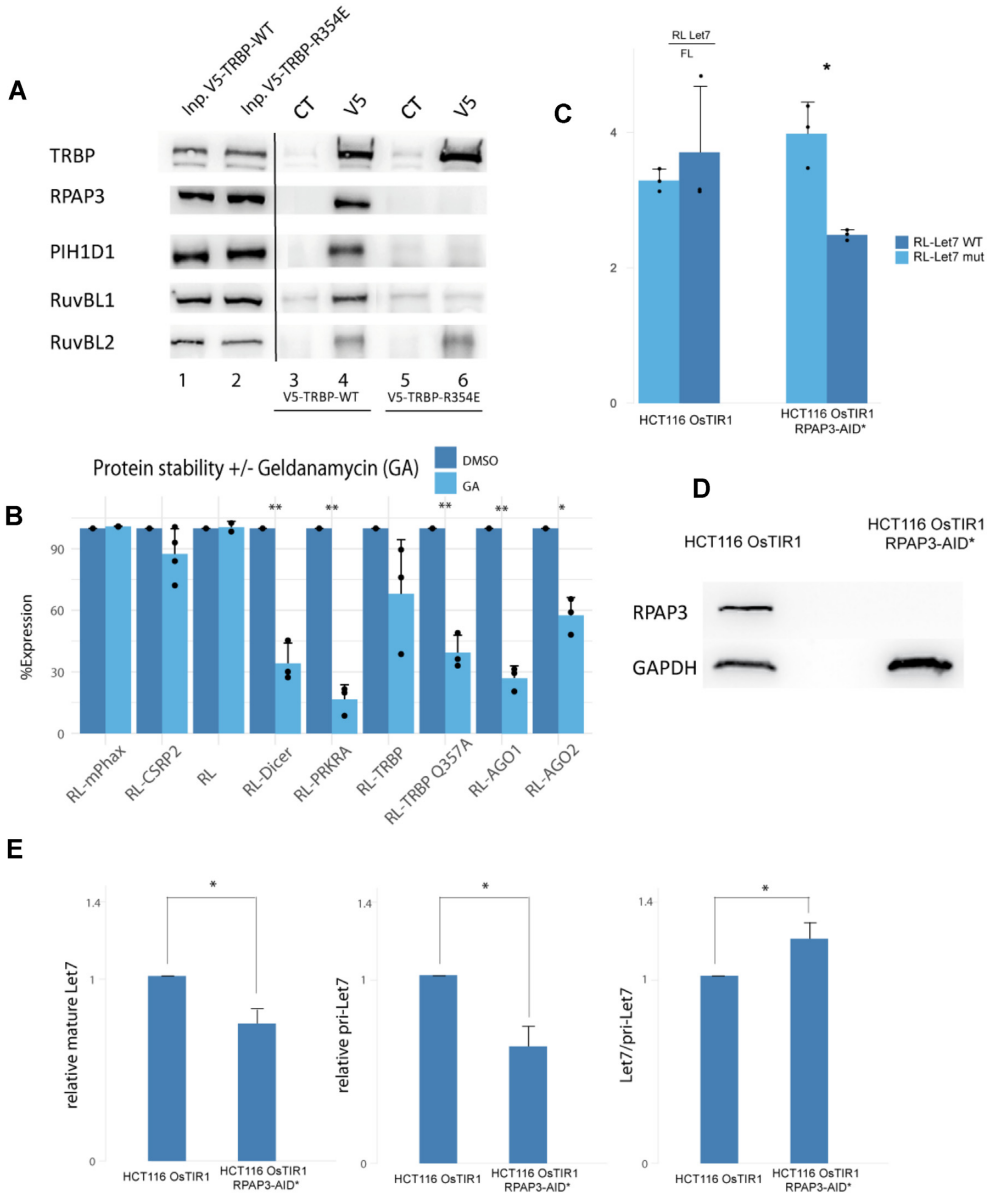

Figure 7. TRBP and Dicer are functionally linked to the R2TP/HSP90 complex. (**A**) Co-immunoprecipitation experiments performed using a transiently expressed V5-tagged TRBP protein, or the TRBP mutant R354E. RPAP3, PIH1D1, RUVBL1 and RUVBL2 are the components of the R2TP complex in human. Antibodies used for the western blot revelation are indicated on the left. V5: IP with the V5 antibody; CT: control IP without antibody. (**B**) Bar plots representing the ratio of HA-Tag Renilla Luciferase (RL) in fusion with the protein of interest and the Firefly Luciferase alone (FL) to show the stability of RL-Dicer, RL-AGO1/2 and RL-TRBP WT/Q357A in 293T cell treated with DMSO or DMSO + 2 μM of Geldanamycin during 16 h. PHAX and CSRP2 are two unrelated protein used as negative controls. * P-value < 0.05. ** P-value < 0.01 according to a Student's test. % expression = 100*(RL-XGA/FLGA) / (RL-XDMSO/FLDMSO). (**C**) Endogenous Let7 dependent translational repression of a Renilla Luciferase reporter was monitored in a control (HCT-116 OsTIR1) versus RPAP3 depleted (HCT-116 OsTIR1 RPAP3-AID*) cell line. WT (RL-Let7 WT) or mutated (RL-Let7 mut) binding sites for the Let7 miRNA were localized in the 3′-UTR of the Renilla luciferase reporter construct. Experiments were performed in triplicate. P-value < 0.01 according to a Student's test. (**D**) Western blot of the control (HCT-116 OsTIR1) versus RPAP3 depleted (HCT-116 OsTIR1 RPAP3-AID*) cell lines, both after Auxin induction, shows complete degradation of RPAP3 in the HCT-116 OsTIR1 RPAP3-AID* cell line. GAPDH was blotted as a control. (**E**) Quantification of mature Let7 miRNA (left panel) and pri-Let7 (middle panel) by RT-qPCR in RPAP3 depleted cells (HCT-116 OsTIR1 RPAP3-AID* + Auxin), compared to control cells (HCT-116 OsTIR1 + Auxin). Results were normalized to the endogenous control U6 snRNA and relative expression levels were calculated using the ΔΔCT method. Right panel shows the mature Let7/pri-Let7 ratio. Data represented correspond to the arithmetical mean values + SEM ($n = 13$). P-values < 0.05 compared to the control according to a Wilcoxon–Mann–Whitney test.

AGO2 (17,18). Interestingly, the mutant of TRBP that does not bind RPAP3 (TRBP Q357A) was even more affected by Geldanamycin treatment, which suggests a stabilizing role for RPAP3 on TRBP when HSP90 is inhibited.

RPAP3 contributes to miRNA-dependent regulation

Inhibition of HSP90, using Geldanamycin for example, was shown to reduce miRNA and siRNA mediated gene silencing (17,18). Here, in order to study the direct influence of RPAP3, rather than HSP90, on miRNA activity, we investigated the effects of RPAP3 depletion using a miRNA reporter. This reporter encodes Renilla Luciferase (RL) with three bulged binding sites for Let7 miRNA in its 3'-UTR (RL-Let7 WT), with Renilla Luciferase expression levels being inversely proportional to the levels of the Let7 miRNA (51,69). To perform these experiments, we also developed the HCT-116 OsTIR1 cell line carrying a homozygous insertion of an Auxin Inducible Degron in RPAP3 (RPAP3-AID*; see Materials and Methods, Supplementary Figure S8), enabling depletion of RPAP3 upon Auxin induction (Figure 7D, Supplementary Figure S8). As compared to a control reporter carrying point mutations in the Let7 binding sites (RL-Let7 mut), which was expressed at the same levels in both cell lines, we observed that the RL-Let7 WT reporter was repressed by about 30% in RPAP3 depleted cells (HCT-116 OsTIR1 RPAP3-AID*), while in our conditions, it was barely repressed by Let7 in wild-type HCT-116 cells. This is likely due to an excess of the reporter mRNA with regard to the low levels of Let7 in HCT-116 cells (70) (Figure 7C,D). This reflected a slightly increased miRNA activity in the absence of RPAP3, indicating that RPAP3, and by extension R2TP, could have a negative effect on miRNA function. Because the interaction of RPAP3 with TRBP is mutually exclusive from the interaction of TRBP with Dicer, this suggests that RPAP3 may sequester TRBP away from Dicer, thus affecting miRNA maturation and/or subsequent activity (Figure 8). Therefore, we monitored Let7 levels in both control and RPAP3 depleted cells (Figure 7E). While we observe a 30 and 40% decrease in mature Let7 and pri-Let7 levels, respectively, when RPAP3 is depleted (Figure 7E, left and middle panels, compare auxin-treated HCT-116 OsTIR1 RPAP3-AID* with auxin-treated HCT-116 OsTIR1 cells), the ratio of Let7/pri-Let7 shows a 20% increase in mature Let7 production in the RPAP3 depleted cells (Figure 7E, right panel, Let7/pri-Let7), suggesting an increased processing in the absence of RPAP3.

DISCUSSION

RPAP3 binds to TRBP using the same surface as Dicer

Our work identified a yet undescribed direct interaction between RPAP3, a core component of the HSP90/R2TP chaperone system, and TRBP, which, among other functions, is one of two alternative Dicer cofactors. We also showed that RPAP3 and Dicer use the same surface of TRBP for binding and thus that the two interactions were mutually exclusive (Figure 4). This was surprising, as there is no significant similarity between RPAP3 and Dicer, neither at the sequence, nor at the secondary structure, levels. For deeper comparison, we superimposed the RPAP3:TRBP and Dicer:TRBP 3D structures using only atoms from TRBP. As expected, the overall 3D structures of RPAP3 and Dicer do not superimpose to each other and the superimposition revealed no significant conformational modifications of TRBP whether it binds to RPAP3 or to Dicer (Supplementary Figure S5). However, a detailed analysis of both interactions revealed that the central parts of α-helixes α4 from RPAP3 and Dicer are located at the same position on the surface of TRBP (Supplementary Figure S9 a,b). Thus, despite very different overall 3D structures, RPAP3 and Dicer share a similar binding site at the TRBP surface and display a α-helix (named α4 in both proteins) that allows equivalent interactions in both RPAP3:TRBP and Dicer:TRBP complexes. This helix could thus be the key determinant for other uninvestigated protein recruitments by TRBP.

RPAP3 does not interact with PACT unlike Dicer

Dicer can associate with either TRBP or PACT and the Dicer:TRBP and Dicer:PACT complexes selectively contribute to miRNA length and strand selection in mammalian cells. Indeed, TRBP and PACT differentially affect dsRNA structure and orientation on Dicer, resulting in different Dicer pre-miRNAs processing activities (10,12). PACT and TRBP are paralogs and their structural organization are very similar. Indeed, TRBP and PACT bind Dicer in a similar manner and their interactions are mutually exclusive (10). As shown above, RPAP3 share some common structural features with Dicer that allow the binding to TRBP. Our candidate-based yeast-two hybrid screen (Figure 1A) completed by co-expression and co-purification assays in *E. coli* revealed no interaction between RPAP3 and PACT (Supplementary Figure S1d–f). This is surprising based on the high amino-acid sequence identity between the third dsRBD of PACT and its homologous sequence in TRBP (55%). Sequence alignment (Supplementary Figure S9c) reveals that six over nine residues involved in the RPAP3:TRBP interface are strictly conserved between PACT and TRBP. Only residues S320, R353 and R354 in TRBP are substituted for N, H and N in PACT, respectively. As shown above in the RPAP3:TRBP complex, the side chain of S320 of TRBP forms a hydrogen-bond with the side-chain of D150 in RPAP3 (Supplementary Figure S7b). Substitution of S320 in TRBP for N in PACT does not abolish possible hydrogen-bond formation. On the other hand, the positively charged residues R353 and R354 forming ionic interactions at the RPAP3:TRBP interface (Figure 6A) are also respectively substituted for H and N in PACT, abolishing the possibility to form salt bridges. Moreover, residue R354 in TRBP is crucial for binding to both RPAP3 and Dicer. Indeed, the R354E mutation disrupts both complexes. Noticeably, the TRBP variant Q357A still interacts with Dicer while it no longer binds RPAP3. Thus, Dicer can bind wild-type TRBP, TRBP Q357A but not TRBP R354E. However, Dicer is able to bind to PACT where R354 is substituted for N as compared to TRBP. On the other hand, RPAP3 binds wild-type TRBP but not the variants R354E,

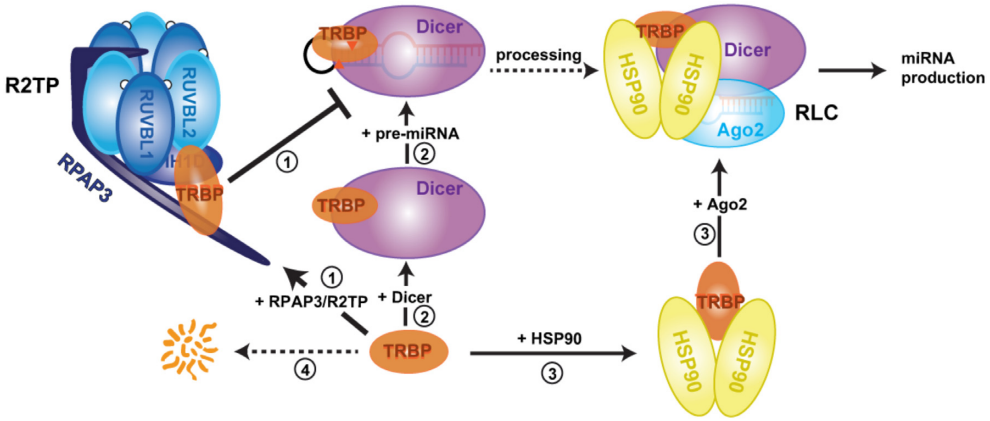

Figure 8. Working model with the hypothetic roles of RPAP3/R2TP and the HSP90 chaperone in the miRNA production pathway. The circled numbers represent the different hypothetical pathways: path 1, RPAP3/R2TP selectively sequesters TRBP; path 2, TRBP directly interacts with Dicer; path 3, HSP90 recruits TRBP and assembles the RLC (RISC (RNA-Induced Silencing Complex) Loading Complex); path 4, TRBP degradation. R2TP is composed of RUVBL1/2, RPAP3 and PIH1D1 proteins.

Q357A and does not bind PACT at all. Altogether, this suggests that substitution of R354 for N in PACT (N301) may be a key point to explain why TRBP binds RPAP3 but PACT does not. Another explanation could be the fact that PACT homodimerizes through its dsRBD3 more strongly than TRBP does, which we observed by NMR and native mass spectrometry (data not shown), thus preventing RPAP3 binding (64).

The mutually exclusive interaction we have described here, between TRBP and RPAP3 versus TRBP and Dicer, associated with the absence of interaction between RPAP3 and PACT, could reveal a putative regulation mechanism of Dicer activity. Indeed, the final processing step of pre-miRNAs by Dicer in the cytoplasm is crucial to generate the proper miRNA ends and thus to specify its mRNA binding properties. PACT and TRBP, the two Dicer partners, have distinct effects on Dicer-mediated dsRNA processing (10,13,65). RNAs processed from long dsRNAs are for example not loaded by PACT, while TRBP handles both pre-miRNA and long dsRNAs. It was also shown that Dicer differentially generated isomiRs depending on its association to TRBP, PACT or none of them (10). Regulation of TRBP binding to Dicer by sequestration by RPAP3 could therefore introduce new biases in miRNA processing, and subsequently mRNA target specificity (Figure 8).

HSP90 controls TRBP and Dicer stabilities, while RPAP3 impedes miRNA processing

We showed that RPAP3, the HSC70/HSP90 chaperones and TRBP co-eluted in co-expression and co-purification experiments (Figure 5). Also, TRBP, probably via RPAP3, co-precipitates all members of the R2TP complex (Figure 7A). Additionally, TRBP and Dicer stabilities decrease in the presence of Geldanamycin, an inhibitor of HSP90, likely leading to reduced miRNA levels (Figure 7B). This is reminiscent of the observation that the activity and localization of AGO2 was previously shown to be dependent on HSP90 (17,18). Finally, we showed that the interactions between TRBP and RPAP3, and between TRBP and Dicer, were mutually exclusive and that depletion of RPAP3 was leading to a 30% increase of Let7 activity (Figure 7C). This suggests a mechanism by which RPAP3 and R2TP could negatively regulate miRNA activity by sequestering TRBP away from Dicer (see model in Figure 8). Consistent with this possibility, we observed that the processing of mature Let7 increased by ∼20% in the absence of RPAP3 (Figure 7E, right panel: Let7/pri-Let7 ratios), which is compatible with the 30% increase of Luciferase repression we observed. However, in RPAP3 depleted cells, we observed overall decreased levels of both mature and pri-Let7 miRNAs (Figure 7E, left and middle panels). This observation suggests that mature Let7 miRNA generated in the absence of RPAP3 is more potent to repress translation of the reporter. This could be due to different mechanisms, such as generation of alternative Let7 (isomiRs) with or without RPAP3, with altered specificity for the target sequence, or by regulating the loading of the processed miRNA on RISC. Additional experiments will be required to determine the precise mechanism of action of RPAP3 on miRNA metabolism. Also, the effects of RPAP3 and of the R2TP complex on endogenous miRNA targets, e.g. Let7 targets, remain to be demonstrated.

Interestingly, the effect of depleting RPAP3 is opposite from what is observed when HSP90 is inhibited (17,18): RPAP3 seems to repress miRNA activity while HSP90 facilitates it. This likely reflects two independent mechanisms: a sequestration of TRBP by RPAP3, while TRBP is stabilized by HSP90, as is AGO2 (Figure 8). Interestingly, as already described for the R2TP complex (71,72), this could suggest an oncogenic function for RPAP3, which could regulate the activity of tumor suppressor miRNAs, such as Let7, in colorectal cancer (70,73). Indeed, downregulation of Let7 has been reported in cells of colorectal cancer patients, together with upregulation of Let7 targets such as LIN28 or HMGA2 (70), while high RPAP3 levels in tumors from patients are associated to bad prognosis (73), which is compatible with the possible regulation model we propose. In the future, it will be interesting to characterize in detail the ef-

fect of RPAP3 on the entire repertoire of miRNAs, isomiRs generation, as well as on other dsRNAs.

DATA AVAILABILITY

The TRBP-dsRBD3:RPAP3-TPR1 complex coordinates and structure factors have been deposited in the PDB with accession code 6ZBK.

SUPPLEMENTARY DATA

Supplementary Data are available at NAR Online.

ACKNOWLEDGEMENTS

We are thankful to Sébastien Pfeffer, Natacha Dreumont, Nicolas Leulliot, Christine Allmang and members of the IMoPA team 1 for helpful discussions. Financial support from the IR-RMN-THC Fr3050 CNRS for conducting the research is gratefully acknowledged.
We thank the platforms 'Biophysique et Biologie Structurale' (B2S) and 'Imagerie et de Biophysique Cellulaire' (PTIBC) of UMS 2008 IBSLor/US40 for access to X-ray crystallography, NMR facilities and confocal microscopes. We are grateful to the synchrotron ESRF (Grenoble, France) for access to the ID29 beamline.
IRCM Cell Culture Unit is acknowledged for the HCT-116 RPAP3-AID* cell line generation.
Séverine Massenet is acknowledged for the PIH1D1 and RUVBL1/2 antibodies.
Author contributions: C.B. and M.R. initiated the project. Y.A., B.C. and M.R. designed the experiments with inputs from all authors. Y.A., V.B-I., M.Q., M-E.C., C.V. and M.R. performed the experiments. M.-C.R. generated the HCT-116 cells lines. C.C. performed the crystallogenesis and the X-ray structural analysis. Y.A. and M.Q. performed the NMR experiments. All authors contributed to data interpretation. Y.A., C.C., E.B., B.C. and M.R. wrote the manuscript with inputs from M.Q., C.V., C.B. and X.M. All authors proofread the manuscript.

FUNDING

Centre National de la Recherche Scientifique; Université de Lorraine; Ministère de l'Enseignement Supérieur, de la Recherche et de l'Innovation MESRI (to Y.A.); Université de Lorraine [CS-UL 2018 AAP-BMS_003_162_INCITATIF_IMoPA_Rederstorff M. to M.R.]; Ligue contre le Cancer; ANRS [20413 AO 2020–2 CSS 11, ECTZ133498]. Funding for open access charge: ANRS [AO 2022-1 CSS 11, ECTZ188028].
Conflict of interest statement. None declared.

REFERENCES

1. Carthew,R.W. and Sontheimer,E.J. (2009) Origins and mechanisms of miRNAs and siRNAs. *Cell*, **136**, 642–655.
2. Bartel,D.P. (2004) MicroRNAs: genomics, biogenesis, mechanism, and function. *Cell*, **116**, 281–297.
3. Gatignol,A., Buckler-White,A., Berkhout,B. and Jeang,K.T. (1991) Characterization of a human TAR RNA-binding protein that activates the HIV-1 LTR. *Science*, **251**, 1597–1600.
4. Dorin,D., Bonnet,M.C., Bannwarth,S., Gatignol,A., Meurs,E.F. and Vaquero,C. (2003) The TAR RNA-binding protein, TRBP, stimulates the expression of TAR-containing RNAs in vitro and in vivo independently of its ability to inhibit the dsRNA-dependent kinase PKR. *J. Biol. Chem.*, **278**, 4440–4448.
5. Komori,C., Takahashi,T., Nakano,Y. and Ui-Tei,K. (2020) TRBP-Dicer interaction may enhance HIV-1 TAR RNA translation via TAR RNA processing, repressing host-cell apoptosis. *Biol. Open*, **9**, bio050435
6. Sanghvi,V.R. and Steel,L.F. (2011) The cellular TAR RNA binding protein, TRBP, promotes HIV-1 replication primarily by inhibiting the activation of double-stranded RNA-dependent kinase PKR. *J. Virol.*, **85**, 12614–12621.
7. Chukwurah,E. and Patel,R.C. (2018) Stress-induced TRBP phosphorylation enhances its interaction with PKR to regulate cellular survival. *Sci. Rep.*, **8**, 1020.
8. Singh,M., Castillo,D., Patel,C.V. and Patel,R.C. (2011) Stress-induced phosphorylation of PACT reduces its interaction with TRBP and leads to PKR activation. *Biochemistry*, **50**, 4550–4560.
9. Ringeard,M., Marchand,V., Decroly,E., Motorin,Y. and Bennasser,Y. (2019) FTSJ3 is an RNA 2'-O-methyltransferase recruited by HIV to avoid innate immune sensing. *Nature*, **565**, 500–504.
10. Wilson,R.C., Tambe,A., Kidwell,M.A., Noland,C.L., Schneider,C.P. and Doudna,J.A. (2015) Dicer-TRBP complex formation ensures accurate mammalian microRNA biogenesis. *Mol. Cell*, **57**, 397–407.
11. Benoit,M.P.M.H., Imbert,L., Palencia,A., Pérard,J., Ebel,C., Boisbouvier,J. and Plevin,M.J. (2013) The RNA-binding region of human TRBP interacts with microRNA precursors through two independent domains. *Nucleic Acids Res.*, **41**, 4241–4252.
12. Lee,H.Y., Zhou,K., Smith,A.M., Noland,C.L. and Doudna,J.A. (2013) Differential roles of human Dicer-binding proteins TRBP and PACT in small RNA processing. *Nucleic Acids Res.*, **41**, 6568–6576.
13. Fareh,M., Yeom,K.-H., Haagsma,A.C., Chauhan,S., Heo,I. and Joo,C. (2016) TRBP ensures efficient dicer processing of precursor microRNA in RNA-crowded environments. *Nat. Commun.*, **7**, 13694.
14. Miyoshi,T., Takeuchi,A., Siomi,H. and Siomi,M.C. (2010) A direct role for hsp90 in pre-RISC formation in drosophila. *Nat. Struct. Mol. Biol.*, **17**, 1024–1026.
15. Iki,T., Yoshikawa,M., Nishikiori,M., Jaudal,M.C., Matsumoto-Yokoyama,E., Mitsuhara,I., Meshi,T. and Ishikawa,M. (2010) In vitro assembly of plant RNA-induced silencing complexes facilitated by molecular chaperone HSP90. *Mol. Cell*, **39**, 282–291.
16. Iwasaki,S., Kobayashi,M., Yoda,M., Sakaguchi,Y., Katsuma,S., Suzuki,T. and Tomari,Y. (2010) Hsc70/Hsp90 chaperone machinery mediates ATP-dependent RISC loading of small RNA duplexes. *Mol. Cell*, **39**, 292–299.
17. Pare,J.M., Tahbaz,N., López-Orozco,J., LaPointe,P., Lasko,P. and Hobman,T.C. (2009) Hsp90 regulates the function of argonaute 2 and its recruitment to stress granules and P-bodies. *Mol. Biol. Cell*, **20**, 3273–3284.
18. Johnston,M., Geoffroy,M.-C., Sobala,A., Hay,R. and Hutvagner,G. (2010) HSP90 protein stabilizes unloaded argonaute complexes and microscopic P-bodies in human cells. *Mol. Biol. Cell*, **21**, 1462–1469.
19. Pare,J.M., LaPointe,P. and Hobman,T.C. (2013) Hsp90 cochaperones p23 and FKBP4 physically interact with hAgo2 and activate RNA interference-mediated silencing in mammalian cells. *Mol. Biol. Cell*, **24**, 2303–2310.
20. Makhnevych,T. and Houry,W.A. (2012) The role of hsp90 in protein complex assembly. *Biochim. Biophys. Acta*, **1823**, 674–682.
21. Cloutier,P., Poitras,C., Durand,M., Hekmat,O., Fiola-Masson,É., Bouchard,A., Faubert,D., Chabot,B. and Coulombe,B. (2017) R2TP/Prefoldin-like component RUVBL1/RUVBL2 directly interacts with ZNHIT2 to regulate assembly of U5 small nuclear ribonucleoprotein. *Nat. Commun.*, **8**, 15615.
22. Boulon,S., Bertrand,E. and Pradet-Balade,B. (2012) HSP90 and the R2TP co-chaperone complex: building multi-protein machineries essential for cell growth and gene expression. *RNA Biol.*, **9**, 148–154.
23. Machado-Pinilla,R., Liger,D., Leulliot,N. and Meier,U.T. (2012) Mechanism of the AAA+ ATPases pontin and reptin in the biogenesis of H/ACA RNPs. *RNA N. Y. N*, **18**, 1833–1845.
24. Boulon,S., Marmier-Gourrier,N., Pradet-Balade,B., Wurth,L., Verheggen,C., Jády,B.E., Rothé,B., Pescia,C., Robert,M.-C., Kiss,T. *et al.* (2008) The hsp90 chaperone controls the biogenesis of L7Ae RNPs through conserved machinery. *J. Cell Biol.*, **180**, 579–595.

25. Bizarro,J., Charron,C., Boulon,S., Westman,B., Pradet-Balade,B., Vandermoere,F., Chagot,M.-E., Hallais,M., Ahmad,Y., Leonhardt,H. *et al.* (2014) Proteomic and 3D structure analyses highlight the C/D box snoRNP assembly mechanism and its control. *J. Cell Biol.*, **207**, 463–480.
26. Bizarro,J., Dodré,M., Huttin,A., Charpentier,B., Schlotter,F., Branlant,C., Verheggen,C., Massenet,S. and Bertrand,E. (2015) NUFIP and the HSP90/R2TP chaperone bind the SMN complex and facilitate assembly of U4-specific proteins. *Nucleic Acids Res.*, **43**, 8973–8989.
27. Malinová,A., Cvačková,Z., Matějů,D., Hořejší,Z., Abéza,C., Vandermoere,F., Bertrand,E., Staněk,D. and Verheggen,C. (2017) Assembly of the U5 snRNP component PRPF8 is controlled by the HSP90/R2TP chaperones. *J. Cell Biol.*, **216**, 1579–1596.
28. Boulon,S., Pradet-Balade,B., Verheggen,C., Molle,D., Boireau,S., Georgieva,M., Azzag,K., Robert,M.-C., Ahmad,Y., Neel,H. *et al.* (2010) HSP90 and its R2TP/Prefoldin-like cochaperone are involved in the cytoplasmic assembly of RNA polymerase iI. *Mol. Cell*, **39**, 912–924.
29. Cloutier,P., Al-Khoury,R., Lavallée-Adam,M., Faubert,D., Jiang,H., Poitras,C., Bouchard,A., Forget,D., Blanchette,M. and Coulombe,B. (2009) High-resolution mapping of the protein interaction network for the human transcription machinery and affinity purification of RNA polymerase II-associated complexes. *Methods San Diego Calif.*, **48**, 381–386.
30. Zur Lage,P., Stefanopoulou,P., Styczynska-Soczka,K., Quinn,N., Mali,G., von Kriegsheim,A., Mill,P. and Jarman,A.P. (2018) Ciliary dynein motor preassembly is regulated by wdr92 in association with HSP90 co-chaperone, R2TP. *J. Cell Biol.*, **217**, 2583–2598.
31. Fabczak,H. and Osinka,A. (2019) Role of the novel hsp90 co-chaperones in dynein arms' preassembly. *Int. J. Mol. Sci.*, **20**, 6174–6188.
32. Hořejší,Z., Stach,L., Flower,T.G., Joshi,D., Flynn,H., Skehel,J.M., O'Reilly,N.J., Ogrodowicz,R.W., Smerdon,S.J. and Boulton,S.J. (2014) Phosphorylation-dependent PIH1D1 interactions define substrate specificity of the R2TP cochaperone complex. *Cell Rep.*, **7**, 19–26.
33. Kim,S.G., Hoffman,G.R., Poulogiannis,G., Buel,G.R., Jang,Y.J., Lee,K.W., Kim,B.-Y., Erikson,R.L., Cantley,L.C., Choo,A.Y. *et al.* (2013) Metabolic stress controls mTORC1 lysosomal localization and dimerization by regulating the TTT-RUVBL1/2 complex. *Mol. Cell*, **49**, 172–185.
34. Takai,H., Xie,Y., de Lange,T. and Pavletich,N.P. (2010) Tel2 structure and function in the Hsp90-dependent maturation of mTOR and ATR complexes. *Genes Dev.*, **24**, 2019–2030.
35. Horejsí,Z., Takai,H., Adelman,C.A., Collis,S.J., Flynn,H., Maslen,S., Skehel,J.M., de Lange,T. and Boulton,S.J. (2010) CK2 phospho-dependent binding of R2TP complex to TEL2 is essential for mTOR and SMG1 stability. *Mol. Cell*, **39**, 839–850.
36. Sugimoto,K. (2018) Branching the tel2 pathway for exact fit on phosphatidylinositol 3-kinase-related kinases. *Curr. Genet.*, **64**, 965–970.
37. Houry,W.A., Bertrand,E. and Coulombe,B. (2018) The PAQosome, an R2TP-Based chaperone for quaternary structure formation. *Trends Biochem. Sci.*, **43**, 4–9.
38. Pal,M., Morgan,M., Phelps,S.E.L., Roe,S.M., Parry-Morris,S., Downs,J.A., Polier,S., Pearl,L.H. and Prodromou,C. (2014) Structural basis for phosphorylation-dependent recruitment of tel2 to hsp90 by pih1. *Struct. Lond. Engl. 1993*, **22**, 805–818.
39. Muñoz-Hernández,H., Pal,M., Rodríguez,C.F., Fernandez-Leiro,R., Prodromou,C., Pearl,L.H. and Llorca,O. (2019) Structural mechanism for regulation of the AAA-ATPases RUVBL1-RUVBL2 in the R2TP co-chaperone revealed by cryo-EM. *Sci. Adv.*, **5**, eaaw1616.
40. Henri,J., Chagot,M.-E., Bourguet,M., Abel,Y., Terral,G., Maurizy,C., Aigueperse,C., Georgescauld,F., Vandermoere,F., Saint-Fort,R. *et al.* (2018) Deep structural analysis of RPAP3 and PIH1D1, two components of the HSP90 Co-chaperone R2TP complex. *Struct. Lond. Engl. 1993*, **26**, 1196–1209.e8.
41. Back,R., Dominguez,C., Rothé,B., Bobo,C., Beaufils,C., Moréra,S., Meyer,P., Charpentier,B., Branlant,C., Allain,F.H.-T. *et al.* (2013) High-resolution structural analysis shows how tah1 tethers hsp90 to the R2TP complex. *Struct. Lond. Engl. 1993*, **21**, 1834–1847.
42. Chagot,M.-E., Jacquemin,C., Branlant,C., Charpentier,B., Manival,X. and Quinternet,M. (2015) (1)H, (15)N and (13)C resonance assignments of the two TPR domains from the human RPAP3 protein. *Biomol. NMR Assign.*, **9**, 99–102.
43. Maurizy,C., Quinternet,M., Abel,Y., Verheggen,C., Santo,P.E., Bourguet,M., Paiva,A.C.F., Bragantini,B., Chagot,M.-E., Robert,M.-C. *et al.* (2018) The RPAP3-Cterminal domain identifies R2TP-like quaternary chaperones. *Nat. Commun.*, **9**, 2093.
44. Martino,F., Pal,M., Muñoz-Hernández,H., Rodríguez,C.F., Núñez-Ramírez,R., Gil-Carton,D., Degliesposti,G., Skehel,J.M., Roe,S.M., Prodromou,C. *et al.* (2018) RPAP3 provides a flexible scaffold for coupling HSP90 to the human R2TP co-chaperone complex. *Nat. Commun.*, **9**, 1501.
45. Daniels,S.M., Melendez-Peña,C.E., Scarborough,R.J., Daher,A., Christensen,H.S., El Far,M., Purcell,D.F., Lainé,S. and Gatignol,A. (2009) Characterization of the TRBP domain required for dicer interaction and function in RNA interference. *BMC Mol. Biol.*, **10**, 38.
46. Natsume,T., Kiyomitsu,T., Saga,Y. and Kanemaki,M.T. (2016) Rapid protein depletion in human cells by auxin-inducible degron tagging with short homology donors. *Cell Rep.*, **15**, 210–218.
47. Yesbolatova,A., Natsume,T., Hayashi,K.-I. and Kanemaki,M.T. (2019) Generation of conditional auxin-inducible degron (AID) cells and tight control of degron-fused proteins using the degradation inhibitor auxinole. *Methods San Diego Calif.*, **164–165**, 73–80.
48. Diebold,M.-L., Fribourg,S., Koch,M., Metzger,T. and Romier,C. (2011) Deciphering correct strategies for multiprotein complex assembly by co-expression: application to complexes as large as the histone octamer. *J. Struct. Biol.*, **175**, 178–188.
49. Rothé,B., Back,R., Quinternet,M., Bizarro,J., Robert,M.-C., Blaud,M., Romier,C., Manival,X., Charpentier,B., Bertrand,E. *et al.* (2014) Characterization of the interaction between protein Snu13p/15.5K and the Rsa1p/NUFIP factor and demonstration of its functional importance for snoRNP assembly. *Nucleic Acids Res.*, **42**, 2015–2036.
50. Clerget,G., Bourguignon-Igel,V., Marmier-Gourrier,N., Rolland,N., Wacheul,L., Manival,X., Charron,C., Kufel,J., Méreau,A., Senty-Ségault,V. *et al.* (2020) Synergistic defects in pre-rRNA processing from mutations in the U3-specific protein rrp9 and U3 snoRNA. *Nucleic Acids Res.*, **48**, 3848–3868.
51. Pillai,R.S., Bhattacharyya,S.N., Artus,C.G., Zoller,T., Cougot,N., Basyuk,E., Bertrand,E. and Filipowicz,W. (2005) Inhibition of translational initiation by let-7 MicroRNA in human cells. *Science*, **309**, 1573–1576.
52. Clément,T., Salone,V. and Rederstorff,M. (2015) Dual luciferase gene reporter assays to study miRNA function. *Methods Mol. Biol. Clifton NJ*, **1296**, 187–198.
53. Keller,R. (2004) In: *Computer-aided resonance assignment tutorial*. 1st edn. CANTINA, Zürich.
54. Shen,Y., Delaglio,F., Cornilescu,G. and Bax,A. (2009) TALOS+: a hybrid method for predicting protein backbone torsion angles from NMR chemical shifts. *J. Biomol. NMR*, **44**, 213–223.
55. Kabsch,W. (2010) xds. *Acta Crystallogr. D Biol. Crystallogr.*, **66**, 125–132.
56. Winn,M.D., Ballard,C.C., Cowtan,K.D., Dodson,E.J., Emsley,P., Evans,P.R., Keegan,R.M., Krissinel,E.B., Leslie,A.G.W., McCoy,A. *et al.* (2011) Overview of the CCP4 suite and current developments. *Acta Crystallogr. D Biol. Crystallogr.*, **67**, 235–242.
57. McCoy,A.J. (2007) Solving structures of protein complexes by molecular replacement with phaser. *Acta Crystallogr. D Biol. Crystallogr.*, **63**, 32–41.
58. Emsley,P., Lohkamp,B., Scott,W.G. and Cowtan,K. (2010) Features and development of coot. *Acta Crystallogr. D Biol. Crystallogr.*, **66**, 486–501.
59. Vagin,A.A., Steiner,R.A., Lebedev,A.A., Potterton,L., McNicholas,S., Long,F. and Murshudov,G.N. (2004) REFMAC5 dictionary: organization of prior chemical knowledge and guidelines for its use. *Acta Crystallogr. D Biol. Crystallogr.*, **60**, 2184–2195.
60. Laskowski,R.A., MacArthur,M.W., Moss,D.S. and Thornton,J.M. (1993) PROCHECK: a program to check the stereochemical quality of protein structures. *J. Appl. Crystallogr.*, **26**, 283–291.
61. Buchan,D.W.A., Minneci,F., Nugent,T.C.O., Bryson,K. and Jones,D.T. (2013) Scalable web services for the PSIPRED protein analysis workbench. *Nucleic Acids Res.*, **41**, W349–357.

62. Dosztányi,Z., Csizmok,V., Tompa,P. and Simon,I. (2005) IUPred: web server for the prediction of intrinsically unstructured regions of proteins based on estimated energy content. *Bioinform. Oxf. Engl.*, **21**, 3433–3434.
63. Yoshida,M., Saeki,M., Egusa,H., Irie,Y., Kamano,Y., Uraguchi,S., Sotozono,M., Niwa,H. and Kamisaki,Y. (2013) RPAP3 splicing variant isoform 1 interacts with PIH1D1 to compose R2TP complex for cell survival. *Biochem. Biophys. Res. Commun.*, **430**, 320–324.
64. Heyam,A., Coupland,C.E., Dégut,C., Haley,R.A., Baxter,N.J., Jakob,L., Aguiar,P.M., Meister,G., Williamson,M.P., Lagos,D. *et al.* (2017) Conserved asymmetry underpins homodimerization of Dicer-associated double-stranded RNA-binding proteins. *Nucleic Acids Res.*, **45**, 12577–12584.
65. Laraki,G., Clerzius,G., Daher,A., Melendez-Peña,C., Daniels,S. and Gatignol,A. (2008) Interactions between the double-stranded RNA-binding proteins TRBP and PACT define the medipal domain that mediates protein-protein interactions. *RNA Biol.*, **5**, 92–103.
66. Liu,Z., Wang,J., Cheng,H., Ke,X., Sun,L., Zhang,Q.C. and Wang,H.-W. (2018) Cryo-EM structure of human dicer and its complexes with a Pre-miRNA substrate. *Cell*, **173**, 1191–1203.
67. Hallais,M., Pontvianne,F., Andersen,P.R., Clerici,M., Lener,D., Benbahouche,N.E.H., Gostan,T., Vandermoere,F., Robert,M.-C., Cusack,S. *et al.* (2013) CBC-ARS2 stimulates 3′-end maturation of multiple RNA families and favors cap-proximal processing. *Nat. Struct. Mol. Biol.*, **20**, 1358–1366.
68. Giacometti,S., Benbahouche,N.E.H., Domanski,M., Robert,M.-C., Meola,N., Lubas,M., Bukenborg,J., Andersen,J.S., Schulze,W.M., Verheggen,C. *et al.* (2017) Mutually exclusive CBC-Containing complexes contribute to RNA fate. *Cell Rep.*, **18**, 2635–2650.
69. Kim,Y., Yeo,J., Lee,J.H., Cho,J., Seo,D., Kim,J.-S. and Kim,V.N. (2014) Deletion of human tarbp2 reveals cellular microRNA targets and cell-cycle function of TRBP. *Cell Rep.*, **9**, 1061–1074.
70. Mizuno,R., Kawada,K. and Sakai,Y. (2018) The molecular basis and therapeutic potential of let-7 microrna against colorectal cancer. *Can. J. Gastroenterol. Hepatol.*, **2018**, 5769591.
71. Kakihara,Y., Kiguchi,T., Ohazama,A. and Saeki,M. (2020) R2TP/PAQosome as a promising chemotherapeutic target in cancer. *Jpn. Dent. Sci. Rev.*, **56**, 38–42.
72. Kakihara,Y. and Saeki,M. (2014) The R2TP chaperone complex: its involvement in snoRNP assembly and tumorigenesis. *Biomol. Concepts*, **5**, 513–520.
73. Maurizy,C., Abeza,C., Lemmers,B., Gabola,M., Longobardi,C., Pinet,V., Ferrand,M., Paul,C., Bremond,J., Langa,F. *et al.* (2021) The HSP90/R2TP assembly chaperone promotes cell proliferation in the intestinal epithelium. *Nat. Commun.*, **12**, 4810.